Title
Biomimetic Catalysts of Graphene Conjugates and Palladium Nanoparticles

Author
Xue, Teng

Publication Date
2014

Peer reviewed|Thesis/dissertation

UNIVERSITY OF CALIFORNIA

Los Angeles

Biomimetic Catalysts of Graphene Conjugates and Palladium Nanoparticles

A dissertation submitted in partial satisfaction of the

requirements for the degree Doctor of Philosophy

in Materials Science and Engineering

by

Teng Xue

2014

ABSTRACT OF THE DISSERTATION

Biomimetic Catalysts of Graphene Conjugates and Palladium Nanoparticles

by

Teng Xue

Doctor of Philosophy in Materials Science and Engineering

University of California, Los Angeles, 2014

Professor Yu Huang, Chair

Biological systems can often drive complex chemical transformations under mild conditions (e.g., aqueous solution, physiological pH, room temperature and atmospheric pressure), which is difficult to achieve in conventional chemical reactions. This unique ability is generally empowered by a series of synergistic protein catalysts that can facilitate reaction cascades through complex metabolic pathways. There is significant interest in exploring molecular assemblies and/or conjugated catalytic systems as analogs to the functional proteins that can facilitate chemical transformation under biologically mild conditions. Hemin, the catalytic center for many protein families including cytochromes, peroxidases, myoglobins and hemoglobins, can catalyze a variety of oxidation reactions like peroxidase enzymes. However, direct application of hemin as an

oxidation catalyst is a significant challenge because of its molecular aggregation in aqueous solution to form catalytic inactive dimers and oxidative self-destruction in the oxidizing media, which causes passivation of its catalytic activity. In the first part of my thesis, we employed the graphene supported hemin as a high efficient peroxidase-mimic catalyst, showing with exceptionally high catalytic activity (k_{cat}) and substrate binding affinity (K_M) approaching that of natural enzymes. The second part of my thesis, we conjugate enzymatic catalyst glucose oxidase (GOx) to the graphene-hemin conjugate. The graphene-hemin-GOx catalyst can readily enable the continuous generation of nitroxyl, an antithrombotic species, from physiologically abundant glucose and L-arginine. We also demonstrate the conjugates can be embedded within polyurethane to create a novel, long-lasting antithrombotic coating for blood contacting biomedical devices. The last part of my thesis, we developed palladium particles with specially engineered ligands to mimic the catalytic cycle of hemin using oxygen as oxidant for ketone dehydrogenative oxidation reaction. By varying the ligands, yield was optimized to 93%, much higher than 1.5% reported previously, exhibiting good heterogeneity and recyclability. Systematic mechanistic studies demonstrate that the ligands can significantly impact on the reaction pathway to modify the catalytic activity and stability. The resulted heterogeneous catalysts also present also have far better activity and stability than homogenous Pd(II) catalysts in high turnover conditions. The novel design on the above biomimetic catalysts have contributed to advancing the synthesis methods and fundamental understandings of heterogeneous catalysts, impacting many applications such as biomedical devices and green chemistry.

The dissertation of Teng Xue is approved.

Xiangfeng Duan

Bruce S. Dunn

Richard B. Kaner

Yu Huang, Committee Chair

University of California, Los Angeles

2014

Table of Contents

List of figures

Acknowledgements

First of all, my doctoral committee Professor Bruce Dunn and Professor Richard Kaner gave me valuable advices in my dissertation. I sincerely appreciate for their help. My advisor, Professor Yu Huang and Professor Xiangfeng Duan spent lots of time and effort training me on how to formulate an idea and push it forward. They also educate me throughout my whole graduate study on how to be creative while collaborative. I couldn't be luckier to have both of them as my advisor and mentor. It's them who made my graduate study a highlighted chapter in my life. I also want to give my special thank to Professor Mark Meyerhoff in University of Michigan. He always gave me overwhelming ideas and unconditional support. Without his help, I cannot move this far. My lab members, each and every one of them, are the ones who helped me out whenever there was a problem. My collaborators Dr. Bo Peng and Dr. Si Yang in Meyerhoff Lab, Dr. Min Xue in Zink Lab, Dr. En-Wei Lin in Maynard Lab and Dr. Sergey Dubin in Kaner Lab are the ones who made the work possible. I also would like to thank Dr. Greg Khitrov, who helped me a lot with GC-MS and LC-MS. Last but not least, I sincerely want to thank my family and my friends for their unconditional love and support.

Biography

Teng Xue received his B.S. degree in Chemistry from Peking University in 2008 and M.S. degree in Chemistry from University of Michigan Ann Arbor respectively. He joined Professor Yu Huang's group in 2010 co-advised by Professor Xiangfeng Duan, in the department of Materials Science and Engineering, University of California Los Angeles. He has three first-author papers including *Nature Communications*, *Angewandte Chemie etc.* and four co-author papers published in peer-review journals. His work have been featured as covers of the published journals and highlighted by media including *Chemical and Engineering News (C&EN)*, *UCLA Newsroom*, *World Journal*, *etc*. He gave oral presentation in Spring 2014 ACS National Meeting in Dallas. His research interests include bimimetic catalysts of graphene conjugates and palladium nanoparticles.

Chapter I: GRAPHENE SUPPORTED HEMIN AS A HIGHLY ACTIVE BIOMIMETIC CATALYST

A. Introduction

Using synthetic systems to mimic natural enzymes with high catalytic activity and distinct substrate selectivity has been a challenge for the last several decades. Hemin, the catalytic center for many protein families including cytochromes, peroxidases, myoglobins and hemoglobins, can catalyze a variety of oxidation reactions like peroxidase enzymes[1]. However, direct application of hemin as an oxidation catalyst is a significant challenge because of its molecular aggregation in aqueous solution to form catalytic inactive dimers and oxidative self-destruction in the oxidizing media, which causes passivation of its catalytic activity[2]. A potential solution to this problem is to synthetically modify the porphyrin structure to achieve a variety of iron porphyrin derivatives for improved catalytic activity or stability[3,4]. An alternative approach is to use high surface area materials such as zeolites, nanoparticles, silica or natural clay to support hemin to achieve improved stability or activity in epoxidation or other reactions in organic solutions[5]. For reactions in aqueous solutions, hydrogel-embedded hemin[6,7] or more elaborate hemin complex obtained by conjugating with specific antibodies[8] have shown activity significantly better than free molecules, which is, however, still orders of magnitude inferior to natural enzymes, not to mention the difficulty in synthesis of such kinds of complex hemin conjugates. Therefore, the discovery and development of novel materials as supports to achieve biomimetic catalysts with enzyme-like activity is highly desired.

Graphene, a single layer of carbon arranged in a honeycomb structure, has attracted intense interest due to its fascinating electronic, thermal, and mechanical properties[10-13]. Graphene is typically prepared through mechanical cleavage or chemical methods[14-16]. In particular, chemical exfoliation of graphite oxide (GO) either by ultrasonic dispersion or rapid thermal expansion followed by chemical reduction provides a low-cost and scalable method to produce bulk quantities of graphene flakes for wide range of applications[17-22]. The resulting graphene usually has a rich variety of a surface defects and functional groups such as carboxylic groups enable it to disperse well in aqueous solution[17,18]. With a two-dimensional sheet-like structure, graphene represents an interesting support for molecular catalysts with a large open surface area that is readily accessible to substrates/products with little diffusion barrier, which is distinct from conventional high surface area porous materials. Moreover, graphene also possesses a rich surface chemistry and has the potential to further promote the catalytic activity and stability of the supported molecular systems such as hemin and other porphyrin species through cation-π interactions or π-π stacking. Although the formation of porphyrin-graphene structures[23-25] and their electrochemical applications[26-38] have been reported recently, many of these studies involve catalytically less active dimers and the superior catalytic properties of hemin-graphene comjugates have not yet been adequately explored[28,29].

Here we report the synthesis of a hemin-graphene conjugate (Fig. 1.1) via π-π stacking interactions. Spectroscopic characterizations show that the hemin retains the catalytic active monomer form as in natural enzymes. The catalytic studies show that the hemin-graphene conjugates can function as effective catalysts in pyrogallol oxidation with exceptionally high catalytic activity (k_{cat}) and substrate binding affinity (K_M)

approaching that of natural enzymes. An iron porphyrin derivative, FeTMPyP (tetramethylpyridylporphyrin iron), was also immobilized on graphene with nearly enzyme-like activity, demonstrating the general applicability of graphene as a support for metalloprophyrin species.

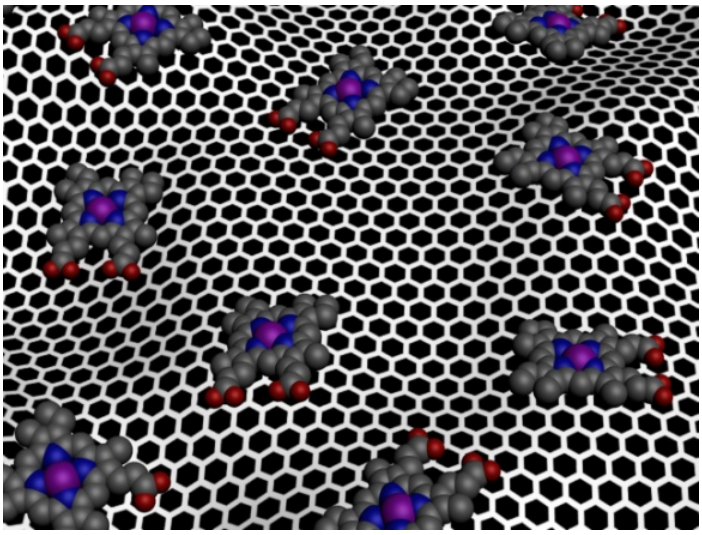

Figure 1.1 Schematic illustration of the formation of hemin-graphene conjugates through π-π stacking.

B. Synthesis and characterization of graphene supported hemin conjugates

Graphene oxide is prepared through Hummer's method[30] and graphene is obtained by reducing graphene oxide with hydrazine[18]. The graphene solution was directly used for the subsequent studies without further purification. Due to the insolubility of hemin in neutral aqueous solution, the conjugation experiments between hemin and graphene were carried out in methanol. The hemin-graphene conjugates were prepared by dispersing dry graphene in 1.5 mM of hemin in methanol followed by incubation for 120 minutes. The hemin-graphene conjugates were then separated from the reaction solution through a

centrifugation process, and characterized using UV-Vis spectroscopy and atomic force microscopy (AFM).

UV-vis absorption spectra of the hemin methanol solution, a mixture of hemin and graphene in methanol, and separated hemin-graphene conjugates re-dispersed in methanol exhibit nearly the same absorption characteristics with a Soret band at 400 nm (Fig. 1.2). The absorption band is consistent with that of monomeric hemin in methanol or dimethyl sulfoxide solution[31], suggesting that the adsorbed hemin species on graphene are monomeric — the same form that hemin takes in natural enzymes. This is also distinct from previous studies on graphene-hemin conjugates, in which hemin dimmers are typically obtained[28,29]. A careful analysis of the spectra reveals that there is some spectral shift in the Q bands and charge transfer band upon the formation of the graphene-hemin conjugate. For example, the Q bands of hemin in the hemin-graphene conjugate blue-shift from 504 nm to 501 nm and 535 nm to 531 nm, respectively, compared to free hemin. The charge transfer band shows an even clearer blue-shift from 628 nm to 623 nm (Fig. 1.3). The band shift suggests the formation of an axial ligation to the iron center of hemin[32] likely due to cation- π interaction between iron centers and graphene.

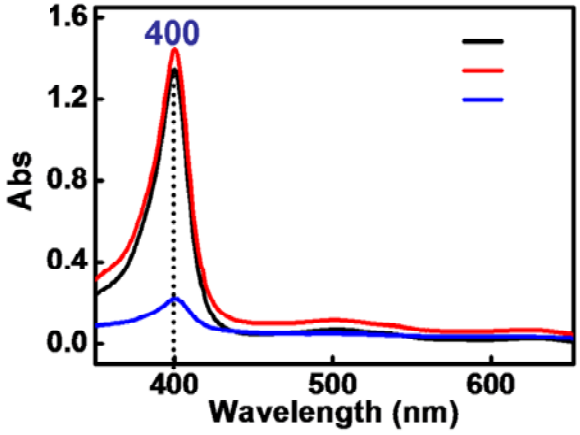

Figure 1.2 UV-vis spectroscopy of free hemin (blue line), hemin/graphene mixture (black line) and separated hemin-graphene re-dispersed in methanol solution (red line). All samples show a Soret band at 400 nm.

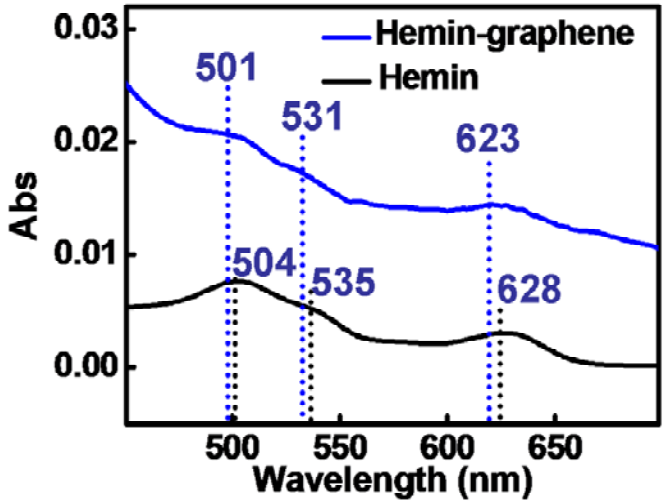

Figure 1.3 UV-vis spectroscopy of free hemin, and a hemin-graphene conjugates in methanol solution shows that the Q bands and charge transfer (CT) band exhibit a slight blue-shift upon formation of hemin-graphene conjugates.

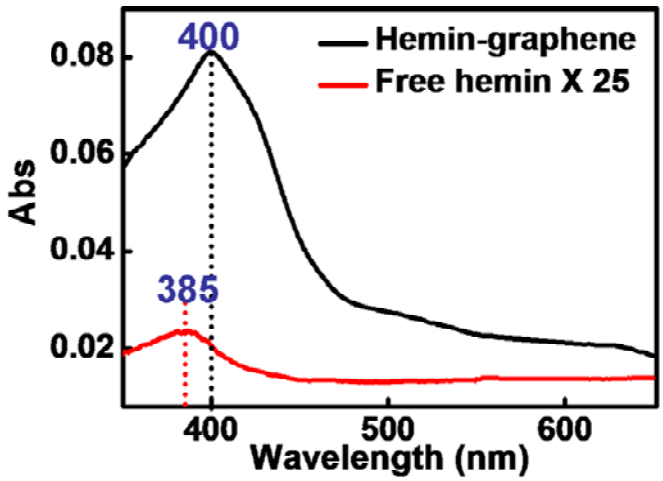

Figure 1.4 UV-vis spectroscopy of free hemin and hemin-graphene conjugates in pH 7.4 Tris buffer, highlighting that hemin-graphene retains its monomeric form, while free hemin in water forms catalytic inactive dimers.

The separated hemin-graphene conjugates were then re-dispersed in pH 7.4 Tris buffer. The equivalent amount of free hemin was also dispersed in pH 7.4 Tris buffer to form a saturated solution. The UV-vis absorption spectra of hemin-graphene conjugates in pH 7.4 Tris buffer show the same absorption peaks as that in methanol, which confirms the structural stability of the hemin-graphene conjugates in pH 7.4 Tris buffer (Fig. 1.4). Quantitative analysis shows that the coverage of hemin on graphene in hemin-graphene conjugates is ~0.3 monolayer. In contrast, the free hemin solution in pH 7.4 Tris buffer shows an extremely weak absorption at 385 nm (Fig. 1.4), indicating the low solubility of hemin and formation of catalytically inactive dimers[33]. XPS studies also confirm the existence of Fe 2p peak, corresponding to iron center in hemin (Fig. 1.5).

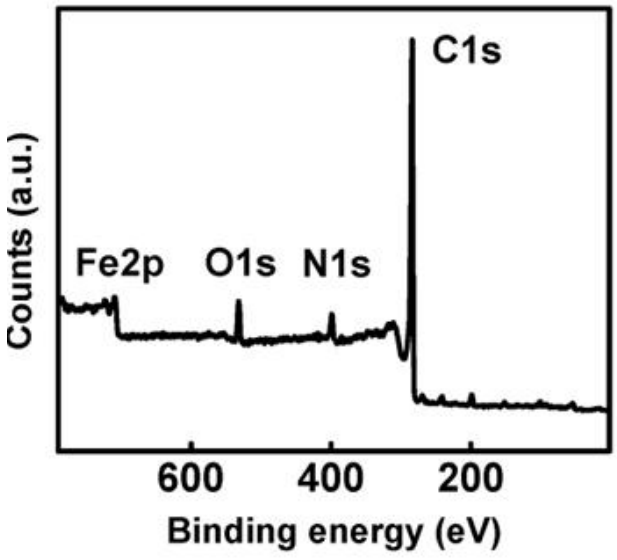

Figure 1.5 XPS study of graphene-hemin conjugates.

The absorption of a monolayer hemin on graphene was also investigated by atomic force microscopy (AFM) studies. Specifically, graphene was first deposited onto silicon oxide substrate from aqueous solution. AFM images were then used to determine the thickness of selected graphene flakes (~1.6 nm for 3-4 layer graphene as shown in Fig. 1.6a and ~1.4 nm for 2-3 layer graphene as shown in Fig. 1.6b). The substrate was then immersed into the hemin methanol solution to allow for absorption of hemin on graphene. The absorption of hemin on a bare silicon oxide substrate is nearly negligible in this process (Fig. 1.7). After absorption, AFM studies show that the thickness of the exact same graphene flakes (~2.0 nm in Fig. 1.6a and ~1.8 nm in Fig. 1.6b, respectively) is increased by ~0.4 nm, which can be attributed to the absorption of a monolayer of hemin molecules on graphene. Control studies conducted by immersing graphene into pure methanol shows no thickness change (Fig. 1.8), confirming that the thickness increase observed above is indeed due to the absorption of hemin on graphene.

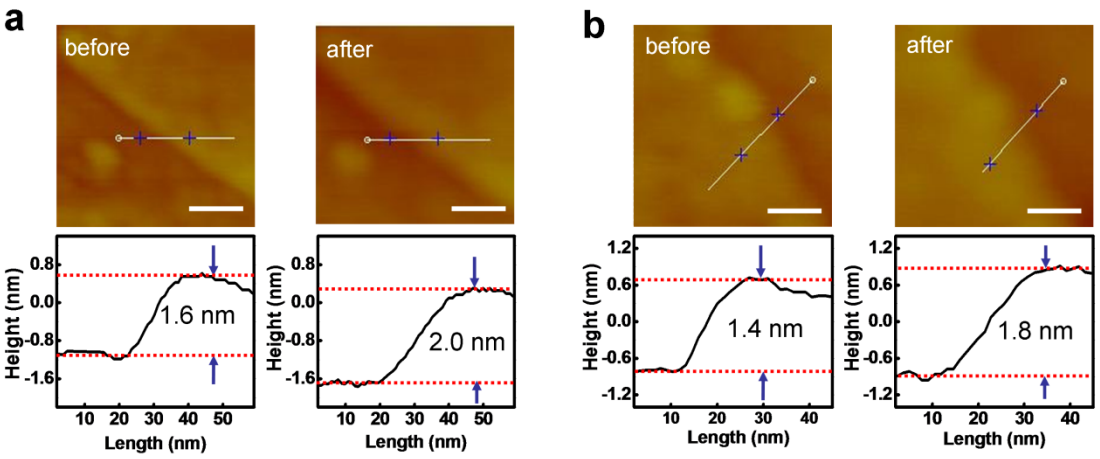

Figure 1.6 AFM morphology for hemin-graphene conjugates. The scale bars are 50 nm. The grahene flakes exhibit a ~0.4 nm increase in step height after immersing into a hemin solution, which can be attributed to the absorption.

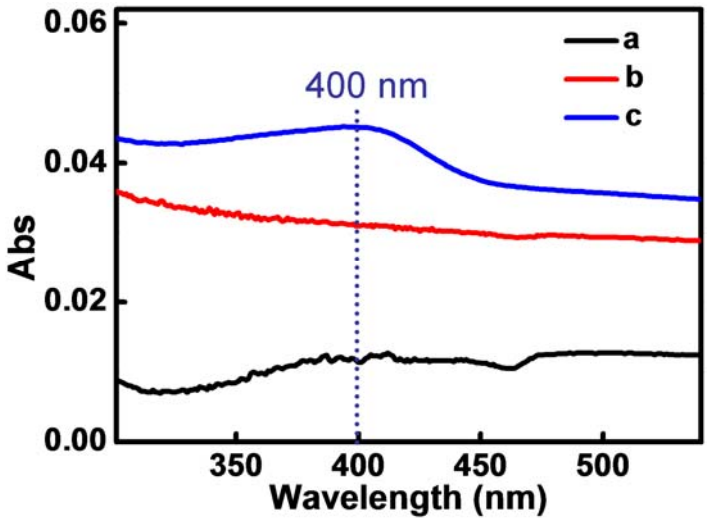

Figure 1.7 UV-vis inspection of hemin on substrate. (a) Hemin absorbed directly on quartz substrate. No obvious Soret band was observed, suggesting little hemin was absorbed on substrate. (b) Graphene absorbed on quartz substrate. (c) Hemin absorbed on quartz substrate with pre-absorbed graphene. Hemin Soret band can be clearly seen at 400 nm, demonstrating the effective absorption of hemin on graphene.

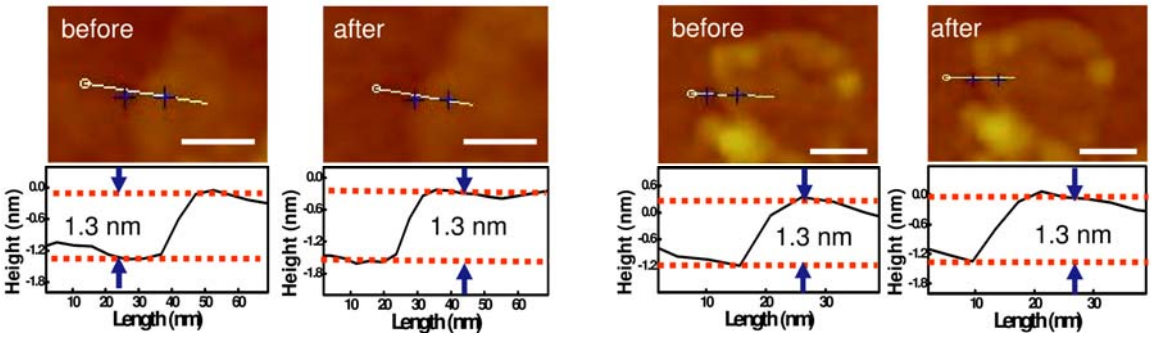

Figure 1.8 AFM morphology of hemin before and after immersed in methanol. The thickness doesn't change. The scale bars are 50nm.

C. Catalytic studies

To evaluate their catalytic activity, hemin-graphene conjugates were used as catalysts for the pyrogallol oxidation reaction (Fig. 1.9a)[6]. The pyrogallol oxidation

reaction is commonly used standard assay to gage the catalytic performance of various porphyrin derivatives[6]. The catalytic reactions were carried out with a constant hemin-graphene catalyst concentration (5 μM hemin equivalent), variable pyrogallol concentrations of 0.1- 2 mM and a hydrogen peroxide concentration of 40 mM. The reaction progress was monitored at 420 nm by kinetic mode UV-vis spectroscopy. The reaction process follows the conventional enzymatic dynamic regulation of the Michiaelis-Menten equation (Fig. 1.9b). Based on the different oxidation rates with variable substrate concentrations, a Lineweaver–Burk plot can be obtained with a near perfectly linear relationship (Fig. 1.9c), from which the important kinetic parameters such as k_{cat} and K_M can be derived (Table 1.1). The k_{cat} gives a direct measure of the catalytic production of the product: i.e, it measures the maximum number of substrate molecules turned over per catalyst molecule per unit time under optimal conditions. It can also be viewed as the optimum turnover rate. K_M is the Michaelis constant and is often associated with the affinity of the catalyst molecules with the substrate. K_M is also a measure of the substrate concentration required for effective catalysis to occur. In this way, k_{cat}/K_M gives a measure of the catalytic efficiency. Either a large value of $k_{\mathbf{cat}}$ (rapid turnover) or a small value of K_M (high affinity for substrate) will make k_{cat}/K_M large enough to obtain improved catalyst efficiency. The derived k_{cat} of the hemin-graphene catalyst shows a surprisingly high value of 246 min^{-1}, which is more than one order of magnitude higher than a recently reported hemin-hydrogel catalyst (19 min^{-1}) and about two orders of magnitude higher than free hemin (2.4 min^{-1}) (Table 1). This K_{cat} value is comparable with that of the natural enzyme horseradish peroxidase (HRP). The derived K_M value (~1.2 mM) is also comparable to that of the natural enzyme HRP (0.81 mM), indicating

good affinity of substrate to the hemin-graphene conjugates. Together, these studies clearly demonstrate that the hemin-graphene catalyst exhibits excellent catalytic efficiency ($k_{cat}/K_M \sim 2\times10^5$), approaching that of the natural enzyme HRP ($k_{cat}/K_M \sim 2\times10^6$).

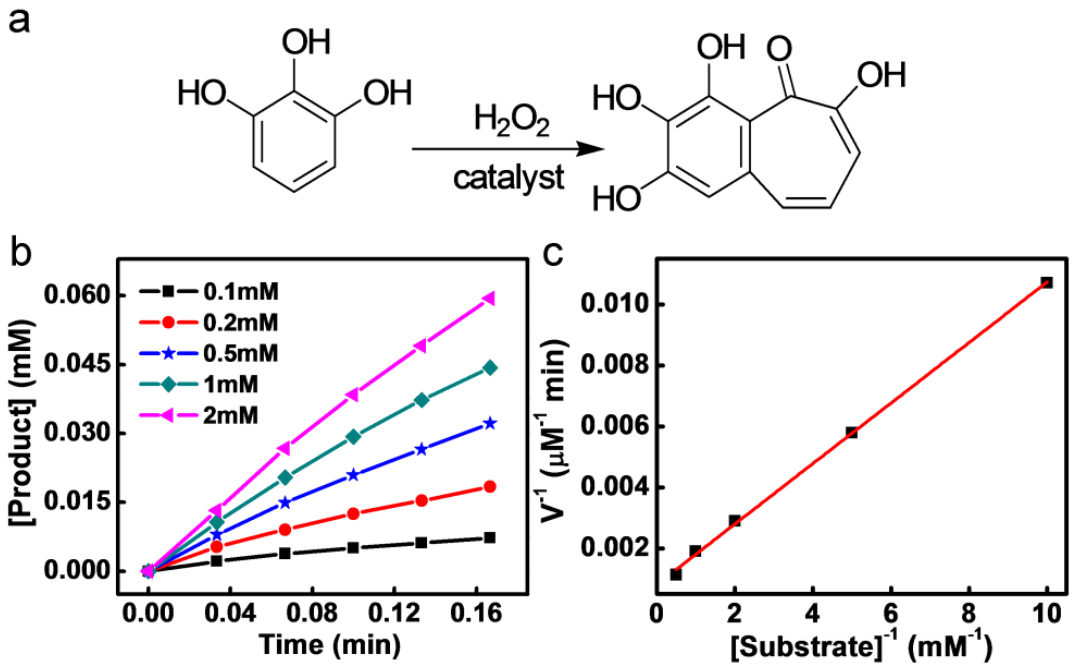

Figure 1.9 Pyrogallol oxidation reaction catalyzed by hemin-graphene conjugates. (a) Schematic illustration of the pyrogallol oxidation reaction. (b) The initial pyrogallol oxidation profile catalyzed by hemin-graphene conjugates (5 μM hemin equivalent). The concentrations of pyrogallol range from 0.1 mM to 2 mM. (c) Lineweaver–Burk plot of the pyrogallol oxidation catalyzed by the hemin-graphene conjugates.

Other porphyrin derivatives such as FeTMPyP have also been explored as alternatives to hemin molecules with improved catalytic performance[7]. To demonstrate the general applicability of a graphene support to enhance the catalytic performance of porphyrin derivatives, we have synthesized FeTMPyP and immobilized them onto

graphene using a similar method. Catalytic studies of the pyrogallol oxidation reaction with a FeTMPyP-graphene catalyst shows similar behavior to that of the hemin-graphene catalyst (Fig. 1.10a). The Lineweaver–Burk plot (Fig. 1.10b) gives a k_{cat} value of 545 min^{-1}, which is comparable to that of the complex antibody supported species (680 min^{-1}). More notably, the K_M of FeTMPyP-graphene (0.96 mM) is much lower than the antibody supported species (8.6 mM), and is similar to that of the natural enzyme HRP (0.81 mM), thus showing excellent binding affinity. The catalytic efficiency (k_{cat}/K_M) of FeTMPyP-graphene (5.7×10^5 $M^{-1}min^{-1}$) is also about one order of magnitude better than the antibody supported species (7.9×10^4 $M^{-1}min^{-1}$) and is nearly comparable to that of natural enzyme HRP ($k_{cat}/K_M \sim 2\times10^6$). Overall, the FeTMPyP-graphene catalyst shows a further improvement in catalytic performance, closely approaching the natural enzyme systems.

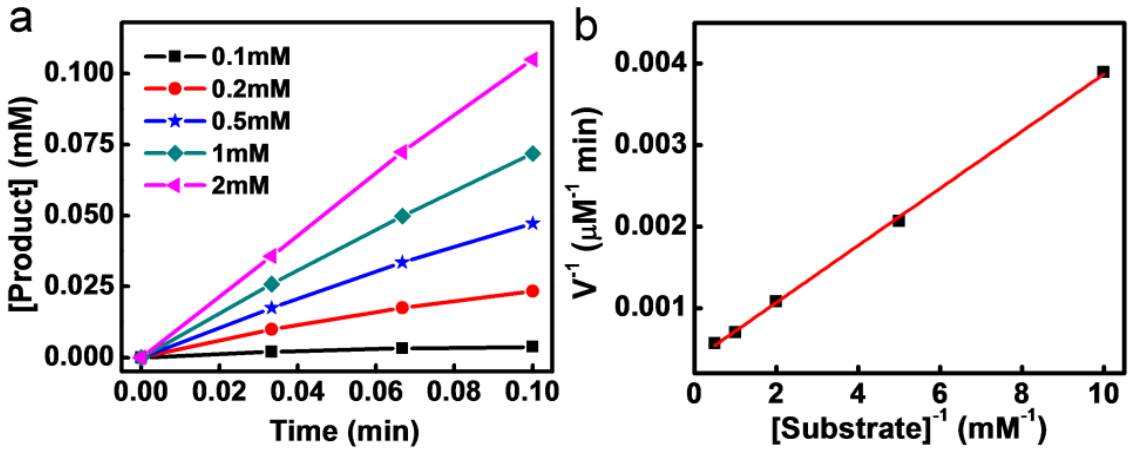

Figure 1.10 Pyrogallol oxidation catalyzed by FeTMPyP-graphene conjugates. (a) Initial pyrogallol oxidation profile catalyzed by FeTMPyP-graphene (5 μM FeTMPyP equivalent). The concentrations of pyrogallol range from 0.1 mM to 2 mM. (b) A Lineweaver–Burk plot of pyrogallol oxidation catalyzed by FeTMPyP-graphene.

Table 1.1 Kinetic parameters for the pyrogallol oxidation reaction catalyzed using different catalysts.

Entry	Catalyst	k_{cat} (min^{-1})	K_M (mM)	k_{cat} / K_M ($M^{-1}min^{-1}$)
1	Hemin-graphene	246	1.22	2.0×10^5
2	Hemin-hydrogel (ref. 6)	19		
3	Hemin (ref.7)	2.4		
4	FeTMPyP-graphene	545	0.96	5.7×10^5
5	FeTMPyP (ref.8)	83		
6	FeTMPyP–antibody (ref.8)	680	8.6	7.9×10^4
7	HRP (ref.8)	1750	0.81	2.2×10^6

D. Discussion and conclusion

Together, our studies clearly demonstrate that graphene supported porphyrin derivatives show excellent catalytic characteristics with generally more than one order of magnitude improvement over other supported systems. The fundamental reason for such a substantial enhancement of catalytic activity is a particularly interesting topic to investigate in the future both experimentally and theoretically. In general, several combined features of the graphene support may contribute to the performance enhancement. First, graphene supported hemin or FeTMPyP could prevent molecules from self dimerizing to form catalytically inactive species. Second, graphene as a support can block one side of the porphyrin molecule which could prevent hydrogen peroxide attack from both sides, and thus lowering the possibility of oxidative destruction of the catalyst molecules themselves[34]. Third, compared to hydrogel support and other three-

dimensional (3D) porous supports, graphene provides a two-dimensional (2D) support with a large open and accessible surface area; therefore, the diffusion of substrate to and product away from the catalytic centers are much easier, which could be beneficial to the reaction turn-over rate and the binding interactions. Previous studies also demonstrated metalloporphyrin immobilized on silica surfaces exhibit a higher catalytic activity than those trapped in a 3D silica matrix[35]. Fourth, graphene as a support could mimic the axial ligation of cysteine or histidine in enzymes due to the cation-π interactions of the iron centers and graphene, which can serve multiple functions to enhance the catalytic characteristics as dictated in previous enzymatic studies[36,37], such as enhancement of the rate of O-O cleavage, promoting heterolytic splitting rather than homolytic O-O splitting[38] and stabilization of the ferryl (FeO^{4+}) moiety due to resonance and enhanced eletrophilicity, which is crucial for catalytic activity[39,40].

Chapter II: INTEGRATION OF MOLECULAR AND ENZYMATIC CATALYSTS ON GRAPHENE FOR BIOMIMETIC GENERATION OF ANTITHROMBOTYIC SPECIES

A. Introduction

In Chapter I, we developed graphene-hemin conjugates and proved it has biomimetic catalytic activity using a model pyrogallol oxidation reaction. In this chapter, we will present a more complex biomimetic reaction that has promising application.

Biological systems can often drive complex chemical transformations under mild conditions (e.g., aqueous solution, physiological pH, room temperature and atmospheric pressure), which is difficult to achieve in conventional chemical reactions. This unique ability is generally empowered by a series of synergistic protein catalysts that can facilitate reaction cascades through complex metabolic pathways. There is significant interest in exploring molecular assemblies and/or conjugated catalytic systems as analogs to the functional proteins that can facilitate chemical transformation under biologically mild conditions[41]. Although "artificial enzymes" have been studied for decades[42], catalysts mimicking true enzymes for designated and complex reaction pathway have been much less frequently explored. The integration of enzymatic catalysts with molecular catalysts could create functional tandem catalytic systems for important chemical transformations not otherwise readily possible[43,44]. Despite the significant interest[45-47], it is quite challenging to build a system that can allow enzymatic catalysts and molecular catalysts to operate synergistically under the same conditions (e.g., aqueous solutions and physiological pH).

Thrombus formation is one of the most common and severe problems that lead to complications of blood-contacting biomedical devices including catheters, vascular grafts and heart valves[48]. Therefore, it is of considerable interest to develop an antithrombotic coating on biomedical devices that can sustain their functionality, decrease failure rate, and thereby greatly reduce associated medical complications and cost. Nitric oxide (NO) is recognized as a potent antiplatelet agent that can help prevent thrombus formation[49]. The extraordinary thrombo-resistant nature of the inner walls of healthy blood vessels is largely attributed to the continuous production of low fluxes (ca. $0.5\sim4.0\times10^{-10}$ mol cm^{-2} min^{-1}) of NO by the endothelial cells (ECs) that line the inner walls of all blood vessels[50]. The design and fabrication of polymeric coatings capable of releasing or generating NO has recently drawn considerable attention for mitigating the risk of thrombus formation. A significant portion of the studies have focused on exogenous NO donors such as diazeniumdiolates (NONOates)[51], which can immediately release NO when exposed to water or physiological environments (i.e., blood, body fluids, *etc.*). Such artificial polymeric coatings with embedded or covalently linked NO donors release NO to minimize thrombus formation[52-54]. However, the application of this approach for long-term implants, such as vascular grafts or hemodialysis catheters, is limited by the inevitable depletion of the finite reservoir of reagents in an exogenous NO donor source[55]. In addition, the labile nature of most NO donors (heat, light, and moisture sensitivity) curtails their practical manufacturability and clinical applications. Moreover, the toxicity of some diazeniumdiolate precursors and the potential formation of carcinogenic nitrosamine byproducts may also pose an adverse effect[56]. Alternatively, a surface coating capable of catalytic generation of NO from physiological components may offer a

more attractive strategy for sustained NO release. For example, organoselenium[57,58] has been shown to trigger the decomposition of *S*-nitrosothiols (RSNO), well known endogenous NO carriers, to generate NO; this strategy is potentially useful for the continuous release of NO over long time periods. However, the relatively low level and highly variable concentrations of endogenous RSNOs in blood[59] limit the reliability of these NO generating materials. *In vivo* toxicity studies also suggested that the reaction between reduced selenium species and oxygen is fast enough to produce a significant amount of superoxide that can react with NO to produce peroxynitrite, a toxic species[60]. In addition, selenium radical formation is also problematic, although aromatic organoselenium species have been found to be far less toxic (e.g., ebselen[61]).

Biologically, NO is believed to arise from the oxidation of L-arginine catalyzed by a family of nitric oxide synthase (NOS) enzymes that utilize the reduced form of nicotinamide adenine dinucleotide phosphate (NADPH) as a cofactor along with O_2 as the oxidant[62,63]. Under conditions where the L-arginine concentration and/or cofactor supplies are limited, nitroxyl (HNO), the one electron reduced form of NO, can also be produced[31]. Nitroxyl has been studied extensively in regard to its provocative and pharmacological importance for heart failure treatment[64], and it has recently been reported that nitroxyl possesses antithrombotic activity analogous to NO[65]. Previous studies also indicate that hydrogen peroxide can substitute for NADPH and O_2 as the oxidant for nitroxyl production[66,67]. Thus biomimetic generation of antithrombotic nitroxyl is a possible solution to the problems associated with NO releasing materials and NO generating catalysts. However, to date, there is no report of a biocompatible surface capable of local generation of nitroxyl for effectively minimizing thrombus formation,

Here we report the immobilization of hemin together with glucose oxidase enzyme (GOx) onto solid graphene supports to create an integrated tandem catalytic system that can make use of endogenous materials in blood for the sustained biomimetic generation of nitroxyl. Hemin, an iron porphyrin species, is the catalytic center of NOS. Free hemin itself is generally inactive as a catalyst because it undergoes molecular aggregation and oxidative destruction under physiological conditions[68]. Resin-supported hydrophilic iron porphyrin derivatives have previously been shown to be active for the oxidation of L-arginine, but with a rather limited turn-over number due to a rapid loss of catalytic activity[69]. This system is also not suitable for practical clinical applications because it requires a high concentration of H_2O_2 oxidant (38 mM), well beyond the physiological concentration. Recent studies have shown that monomeric hemin can be immobilized onto graphene to form a stable graphene-hemin conjugate that exhibits peroxidase-like activity for a variety of biomimetic oxidation reactions, using H_2O_2 as the oxidant[70,71]. In our tandem catalyst system, with the integration of GOx, we expect to produce H_2O_2 locally from endogenous glucose for the subsequent hemin-catalyzed oxidation of L-arginine to generate antithrombotic nitroxyl species.

In this study, we immobilized monomeric hemin onto graphene through π-π interactions and covalently linked GOx with graphene to form a graphene-hemin-GOx conjugate surface (Fig. 2.1). Furthermore, we demonstrate that this complex conjugate can be used as an effective biomimetic catalyst for the generation of nitroxyl species using only endogenous species, namely glucose and L-arginine. Importantly, the physiological concentrations of glucose, L-arginine and the required nitroxyl levels for antiplatelet activity follow a nearly ideal cascade: blood glucose concentration is ca. 2-5

mM, capable of creating more than enough peroxide to oxidize L-arginine, which is present at ca. 200 μM. The amount of nitroxyl necessary for significant antithrombotic effects is likely in the sub-μM range[65], which is at least three to four orders of magnitude lower than actual L-arginine concentrations. We have investigated the nitroxyl production behavior using various methods including FT-IR spectroscopy, GC-MS, fluorescence spectroscopy (DAF assay), and chemiluminescence. Furthermore, a biocompatible polymer film with embedded graphene-hemin-GOx conjugates was prepared, and demonstrated to exhibit greatly enhanced anti-platelet activity due to the continuous generation of nitoxyl.

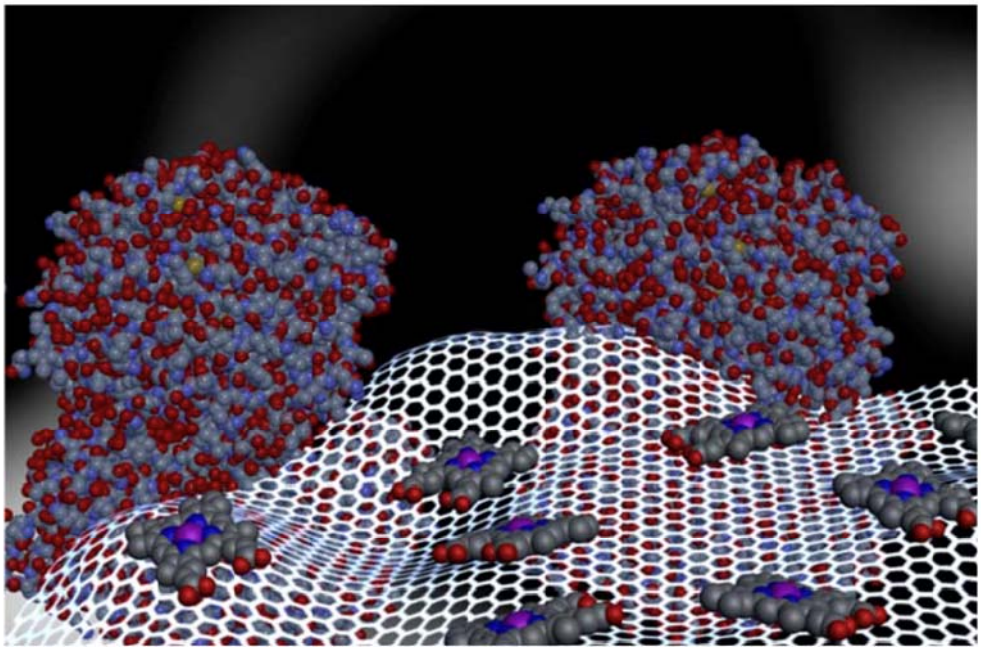

Figure 2.1 Schematic illustration of graphene-hemin-GOx conjugates. Monomeric hemin molecules are conjugated with graphene through π-π interactions to function as an effective catalyst for the oxidation of L-arginine; and GOx is covalently linked to graphene for oxidation of glucose and local generation of H_2O_2.

B. Nitroxyl production by graphene-hemin conjugates

The catalytic oxidation characteristics of graphene-hemin conjugates were initially investigated. Graphene was obtained by hydrazine reduction of exfoliated graphene oxide prepared via Hummer's method[30]. The immobilization of monomeric hemin on graphene via π-π stacking was conducted using our previously reported approach[70]. L-arginine oxidation reactions were conducted by dispersing the graphene-hemin catalyst in a pH 7.4 PBS buffer with 200 μM L-arginine added, along with 5 mM H_2O_2 as the oxidant (Fig. 2.2).

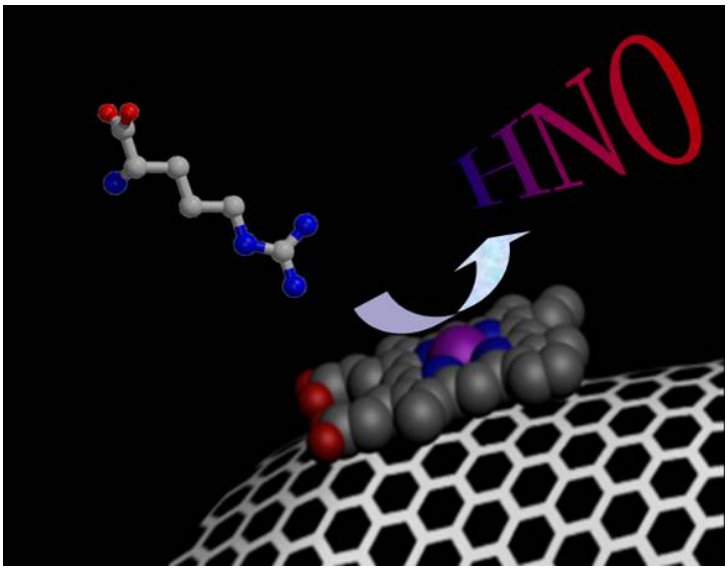

Figure 2.2 A schematic illustration of graphene-hemin catlyzed L-arginine oxidation to produce nitroxyl.

The L-arginine oxidation reaction could potentially result in multiple different products including nitric oxide (NO) or nitroxyl (HNO). We have conducted extensive characterizations to demonstrate the product is predominantly HNO. For product identification, the generated nitroxyl dimerizes to form nitrous oxide over time, which is

detectable by gas phase FT-IR spectroscopy[72]. The gas phase FT-IR spectrum of the headspace gas of reaction vessel confirms the presence of nitrous oxide with two stretching bands at 2211cm^{-1} and 2235 cm^{-1} (Fig. 2.3). The NO stretching bands at 1790cm^{-1} and 1810 cm^{-1} are not observed, excluding NO as the product of the reaction.

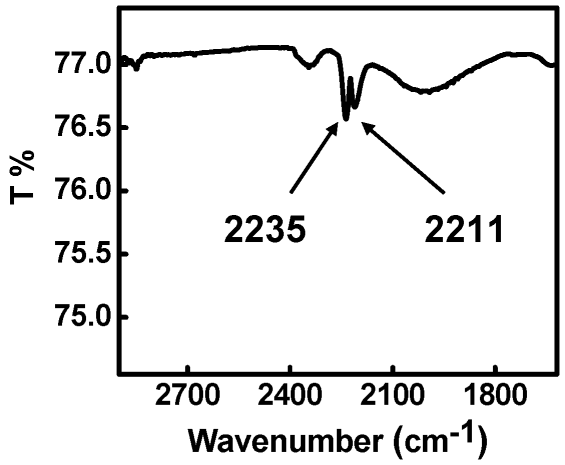

Figure 2.3 FT-IR spectrum of headspace gas from L-arginine oxidation reaction vessel (with graphene-hemin catalysts). Nitrous oxide with two stretching bands at 2211cm^{-1} and 2235 cm^{-1} are present. The NO stretching band at 1790cm^{-1} and 1810 cm^{-1} are not observed.

The headspace gas is also tested by GC-MS for nitrous oxide detection[73], which further proves the existence of nitroxyl (Fig. 2.4). Additionally, chemiluminescence analysis, which can selectively detect ppb levels of NO, but not nitroxyl nor nitrous oxide, also demonstrates that there is no NO produced from the oxidation reaction (Fig. 2.5). The expected byproduct L-citrulline is also tested by LC-MS[74], further confirming the reaction pathway (Fig. 2.6).

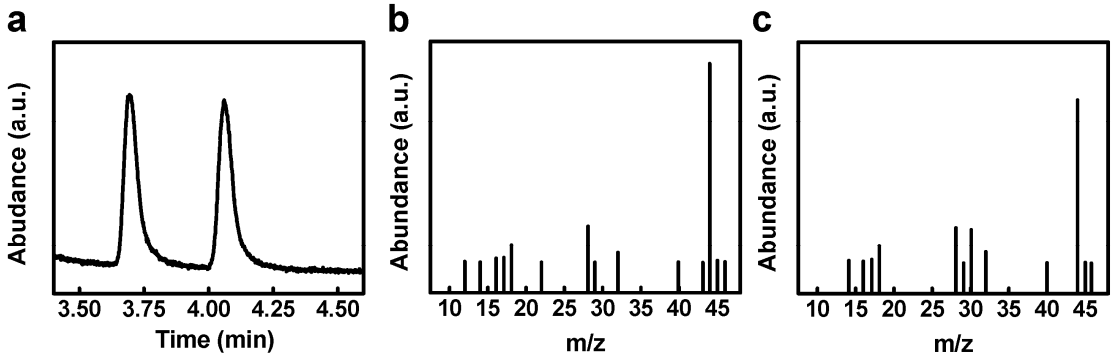

Figure 2.4 GC-MS analysis of headspace gas from L-arginine oxidation reaction vessel (with graphene-hemin catalysts). (a). GC profile of headspace gas. (b). MS profile of headspace gas at retention time of 3.69 min, indicating the presence of CO_2. (c). MS profile of headspace gas at retention time of 4.06 min, indicating the presence of nitrous oxide.

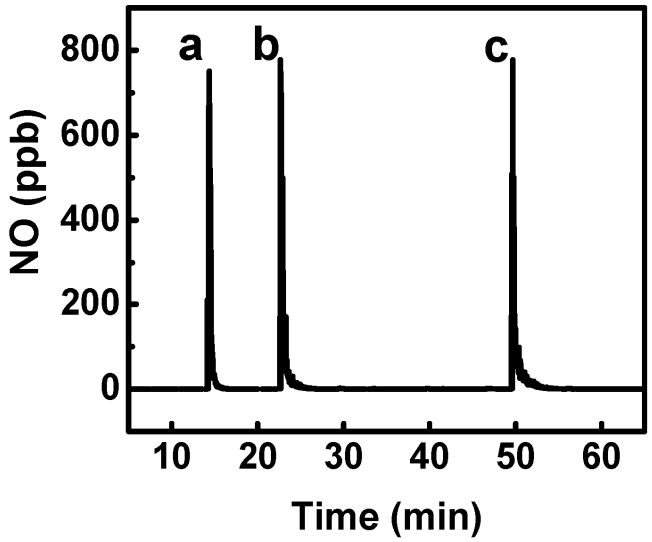

Figure 2.5 Chemiluminescence analysis of the oxidation reaction product and the standard NO solution (a). blank NO solution. (b). NO solution incubated with graphene-hemin conjugates. (c). NO solution incubated with graphene-hemin-GOx conjugates. All the three peaks show the same intensity, demonstrating catalyst conjugates don't trap NO. Chemiluminescence experiments don't show any NO signal from the product of the L-

arginine oxidation catalyzed by our conjugates. Control experiments with standard NO solution with or without the catalyst conjugates show similar intensity, demosntrating that catalyst conjugates also do not trap NO, which further exclude NO as a possible product.

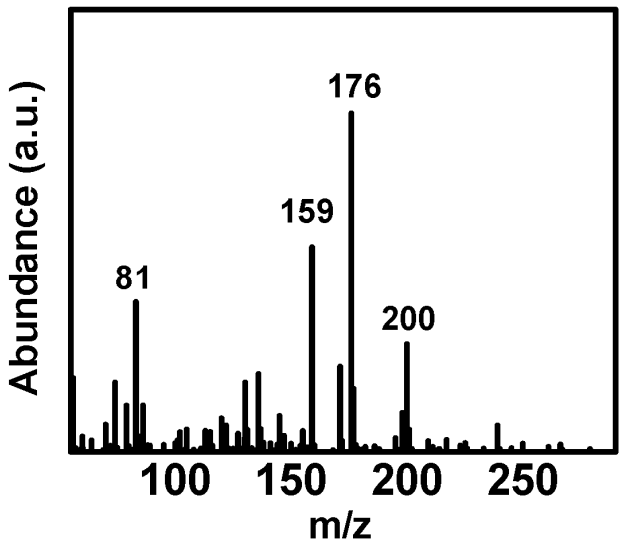

Figure 2.6 MS spectrum of L-citrulline detected by LC-MS. The detected L-citrulline shows a protonated molecular ion peak $[M+H]^+$ (m/z 176), which has the highest abundance, together with several signature peaks.

The above studies demonstrate that a graphene-hemin conjugate can function as an effective catalyst for the production of nitroxyl. However, those methods are not capable of quantifying the generated nitroxyl amount in reaction solution. Therefore, a fluorescence diaminofluorescein (DAF) assay was utilized. It has been documented that nitroxyl can react with DAF-2 to form DAF-triazole with fluorescence emission[75]. The fluorescence spectrum was monitored at different time intervals (Fig. 2.7), and the intensity increase of the emission peak at 515 nm was calibrated with the corresponding nitroxyl concentrations (Fig. 2.8). The DAF assay clearly shows the production of nitroxyl immediately after the introduction of H_2O_2 to a graphene-hemin catalyzed

reaction mixture, while the control reaction without the graphene-hemin conjugate does not yield any signal (Fig. 2.8). Significantly, for the reactions with the equivalent amount of hemin, the graphene-hemin catalysts exhibit a remarkably higher activity, while the free hemin hardly shows any catalytic activity at all (Fig. 2.8). Such a difference in catalytic behavior can likely be attributed to the monomeric molecular structure of hemin on graphene supports. For free hemin, the active catalytic sites are limited due to molecular aggregation of hemin to form inactive dimers. The catalytic turn-over frequency of graphene-hemin is calculated to be 0.015 min^{-1} (Fig. 2.8), which is greatly higher than that of the previously reported resin supported system (0.0016 min^{-1})[69]. Moreover, graphene-hemin conjugates also exhibit exceptional catalytic activity stability, with nearly a constant turnover rate over a 50-minute test period, while the previously reported resin supported hemin could only catalyze the reaction for about 6 min before a total loss of its catalytic activity[69].

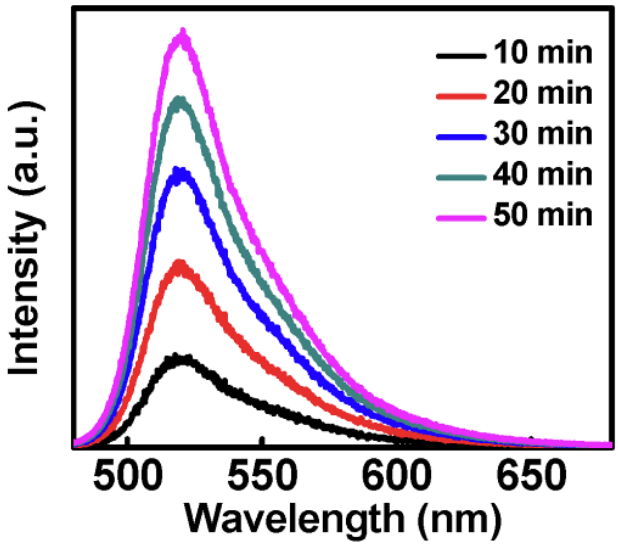

Figure 2.7 Relative fluorescence spectra at different reaction time obtained by DAF Assay.

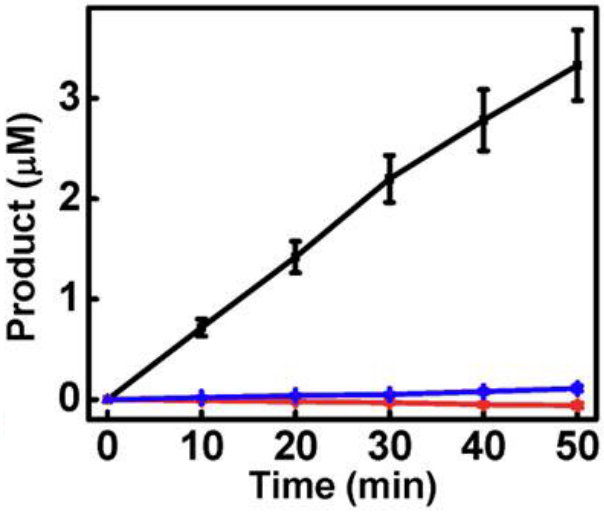

Figure 2.8 The nitroxyl concentration measured using a DAF assay. Black line represents product formation using graphene-hemin conjugate catalyst. Blue line represents product formation using free hemin catalyst. Red line represents product formation in a control experiment without any catalyst.

C. Nitroxyl production by graphene-hemin-GOx conjugates

Although, as demonstrated above, the graphene-hemin conjugates can effectively catalyze the oxidation of L-arginine to generate nitroxyl, this reaction requires a relatively high concentration (~5 mM) of H_2O_2 oxidant that is far above the physiological H_2O_2 concentration (10^{-9} ~ 10^{-7} M)[76]. To apply the graphene-hemin catalyst for practical applications under physiological conditions requires a mechanism to locally produce desired levels of H_2O_2. To this end, linking GOx to the graphene-hemin conjugates can offer an approach to elevate the local H_2O_2 concentration through the oxidation of blood glucose. GOx was anchored via a NHS-EDC coupling reaction and linked to the edge and defect site carboxyl groups of graphene. NHS-EDC coupling has been successfully used

for the covalent linkage of GOx onto graphene oxide previously[77]. Stained TEM shows dark features of around 10 nm size distributed around the edges or defective sites of graphene, which is attributed to the successful linkage of GOx (Fig. 2.9). The formation of graphene-hemin-GOx is also supported by zeta potential measurements (Table 2.1). Once the graphene-hemin-GOx conjugates were obtained, H_2O_2 production activity was tested in the presence of glucose and L-arginine (Fig. 2.10), demonstrating that GOx retains good activity after chemical linkage onto the graphene.

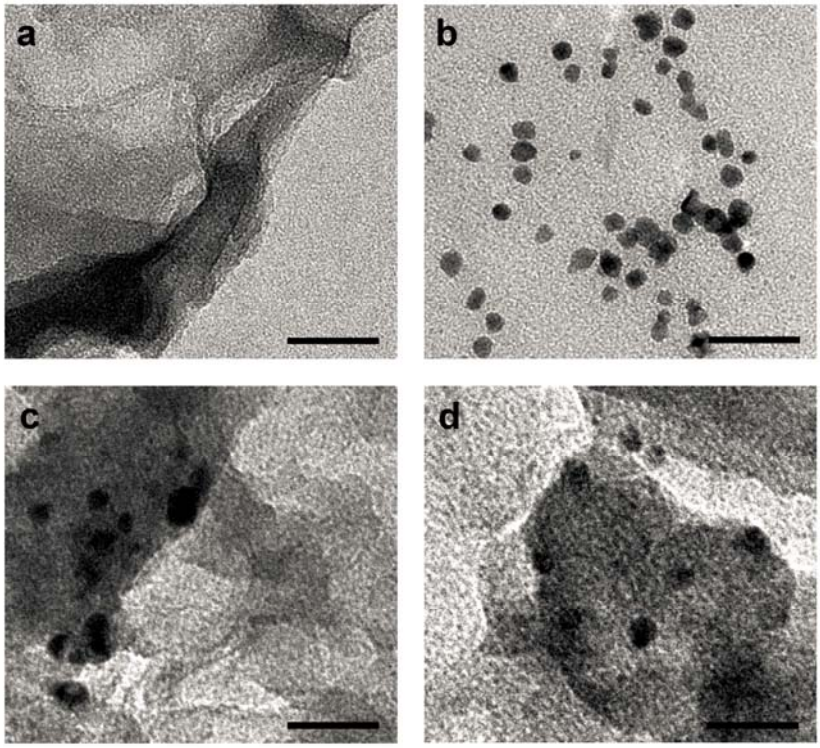

Figure 2.9 Stained TEM images. (a). graphene-hemin. (b). GOx. (c,d). graphene-hemin-GOx. Black features populated on graphene sheets (mostly near the edges) are GOx linked with carboxyl groups around the edge or defect sites of graphene via NHS/EDC coupling. Scale bars are 40 nm.

Table 2.1 Zeta potentials are measured at 25^{o}C in pure water. Graphene-hemin has a more negative potential than graphene, due to the conjugation of negatively charged

hemin. Graphene-hemin-GOx is slightly more negative than graphene-hemin, indicating the successful conjugation of GOx.

Materials	Zeta potential (mV)
GOx	-4.14
graphene	-24.2
graphene-hemin	-28.5
graphene-hemin-GOx	-31.6

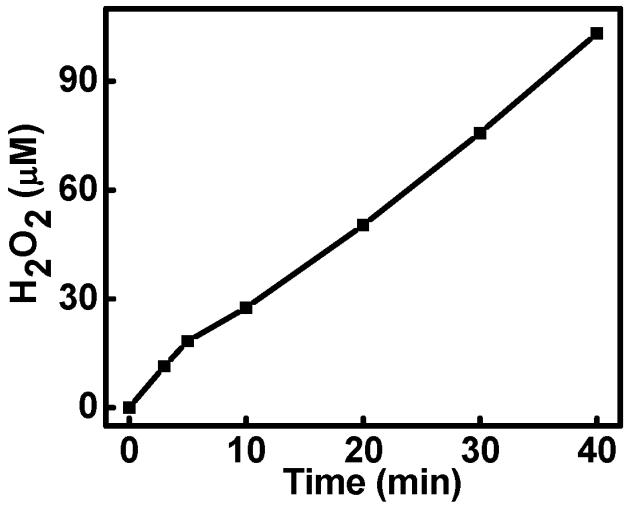

Figure 2.10 H_2O_2 evolution profile of graphene-hemin-GOx. The H_2O_2 production rate is about 0.83 μM/min per mg conjugates.

The integrated catalysts were then used to catalyze the L-arginine oxidation reaction, and the nitroxyl generation behavior was studied using the DAF-based nitroxyl assay. In pH 7.4 PBS buffer containing physiological concentrations of glucose (5 mM) and L-arginine (200 μM), the graphene-hemin-GOx conjugates produce nitroxyl after a short activation stage (~ 5 min) (Fig. 2.11). This lag might be due to the necessary

accumulation of an adequate H_2O_2 concentration at the surface of the graphene. For a series of control experiments, graphene-hemin-GOx catalysts in a solution of only glucose cannot produce any nitroxyl, and a similar result was obtained for a solution containing only L-arginine, but not glucose (Fig. 2.11). In a solution with both glucose and L-arginine, if only graphene-hemin conjugates or graphene-GOx conjugates alone are introduced, no nitroxyl production is observed. Taken together, these findings clearly demonstrate that nitroxyl production is observed only when the graphene-hemin-GOx conjugates, glucose, and L-arginine are all present (Fig. 2.11).

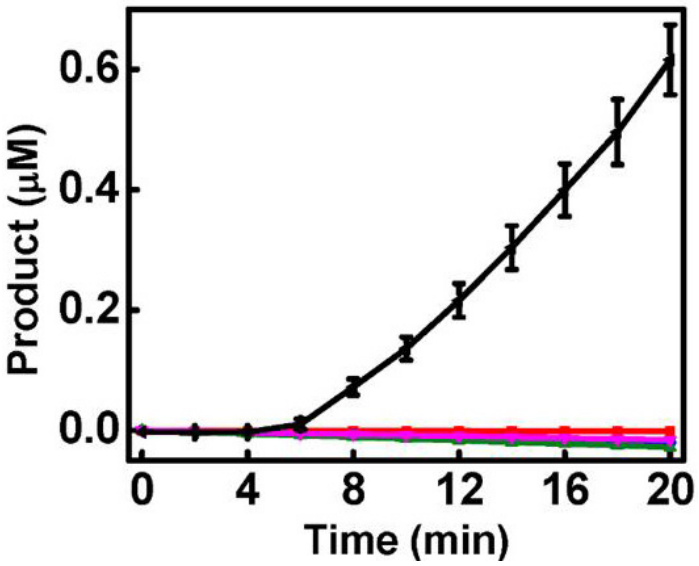

Figure 2.11 Nitroxyl generation of graphene-hemin-GOx and control experiments. The production of nitroxyl was quantified using a DAF assay. Black line, graphene-hemin-GOx in glucose and L-arginine; red line, graphene-hemin in glucose and L-arginine; blue line, graphene-GOx in glucose and L-arginine; green line, graphene-hemin-GOx in glucose; pink line, graphene-hemin-GOx in L-arginine.

The real time reaction behavior of this mixture was also monitored (Fig. 2.12). Overall, the graphene-hemin-GOx conjugates can maintain good and stable activity over an extended period, and exhibits excellent recyclability (Fig. 2.12).

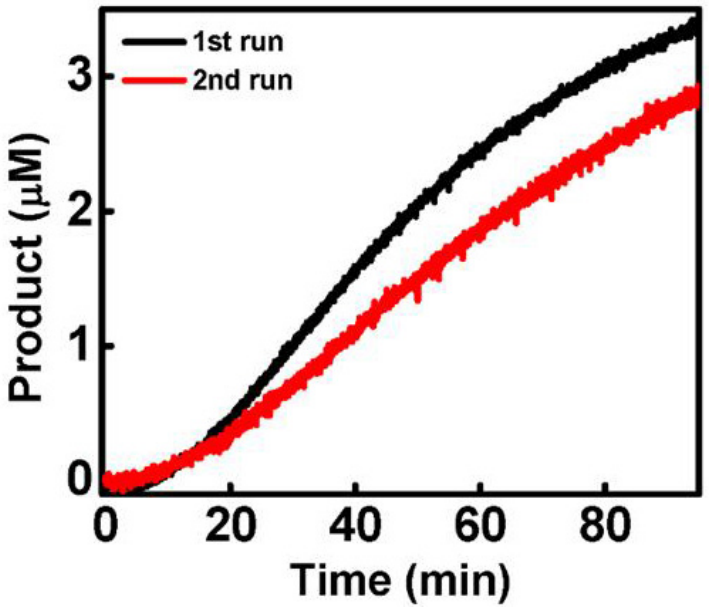

Figure 2.12 Real time nitroxyl production catalyzed by graphene-hemin-GOx (black line) and the recyclability of the graphene-hemin-GOx catalysts (red line).

D. Antithrombotic behavior of graphene-hemin-GOx embedded film.

Our studies have clearly demonstrated that graphene-hemin-GOx conjugates can function as effective catalysts for the generation of nitroxyl with endogenous components. To further investigate whether the graphene-hemin-GOx conjugates can offer an effective solution for potential biomedical applications, we embedded the conjugates (at ~40 wt%) in a commercially available polyurethane (Tecophilic® SP-93A-100) that was then spin-coated to form biocompatible films. Control thin film samples were also prepared with embedded graphene, graphene-hemin or graphene-GOx (at the same wt%). All the films were then immersed into platelet rich rabbit blood plasma for 3 days, and then examined

by SEM to evaluate the platelet adhesion characteristics[78]. Control films containing graphene, graphene-hemin or graphene-GOx exhibited very rough surfaces after blood contact, indicating obvious adhesion of a significant number of blood platelets (Fig. 2.13a-c, e-g). In contrast, the film containing graphene-hemin-GOx shows a minimum morphology change before and after blood contact (Fig. 2.13d,h), clearly demonstrating excellent anti-platelet function.

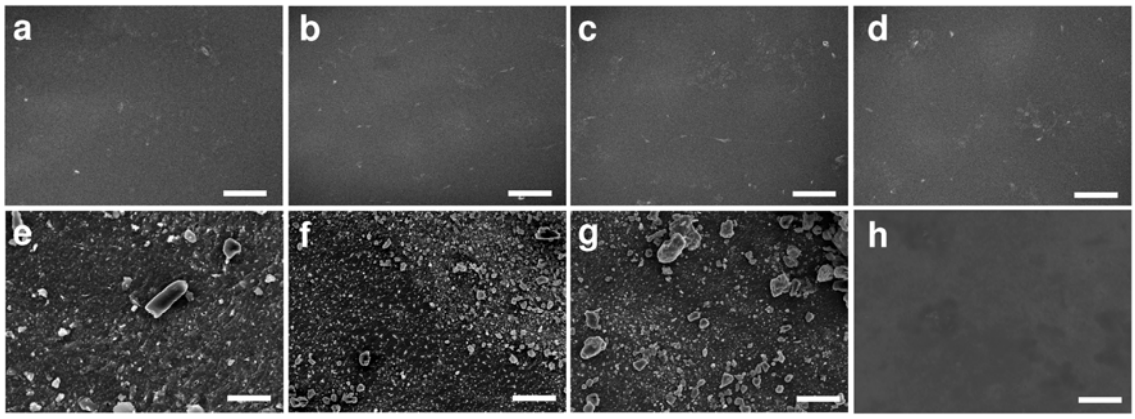

Figure 2.13 Antithrombotic behavior of biocompatible films containing graphene-hemin-GOx conjugates. SEM images of as formed films containing (a). graphene, (b). graphene-hemin, (c). graphene-GOx and (d). graphene-hemin-GOx; and the respective films after immersing into platelet rich rabbit blood plasma for 3 days: (e). graphene, (f). graphene-hemin, (g). graphene-GOx and (h). graphene-hemin-GOx. Only films containing graphene-hemin-GOx exhibit a minimum morphology change by SEM after immersion into blood plasma compared to control films of graphene, graphene-hemin or graphene-GOx. Scale bars are 10 μm.

E. Discussion and conclusion

By simultaneously conjugating hemin and glucose oxidase on graphene, we have created an integrated tandem catalyst that can drive a reaction cascade to allow for *in-situ* generation of H_2O_2 for the oxidation of L-arginine. This process can thus allow sustained generation of nitroxyl from physiological glucose, L-arginine and blood oxygen. The embedment of such tandem catalysts into biocompatible films can create a surface coating with excellent anti-platelet characteristics, offering a potential solution to sustained generation of antithrombotic nitroxyl species on medical devices when in contact with fresh blood. Overall, our studies demonstrate a general strategy to integrate molecular catalysts and enzymatic catalysts on the same platform for them to synergistically facilitate complex reaction pathways under mild physiological relevant conditions, and enable important chemical transformations not otherwise readily possible. It can impact diverse areas including biomedicine and green chemistry.

Chapter III: ENGINEERING MOLECULAR LIGANDS ON PALLADIUM NANOPARTICLES FOR HIGHLY EFFICIENT AND ROBUST HETEROGENEOUS CATALYSIS

A. Introduction

In Chapter I and II, we have discussed using graphene-hemin conjugates or more complex graphene-hemin-GOx conjugates as biomimetic catalysts. However in both of the cases, H_2O_2 has to be used instead of O_2 as oxidant. Using O_2 as the only oxidant is much more desirable due to its abundance. A close look at the catalytic cycle of iron center in hemin revealed that Fe undergoes a two valence charge change during the catalytic reaction (Fig. 3.1a). This process can be mimicked by other metals, such as Pd (Fig 3.1b). In this chapter, we utilize Pd nanoparticles to catalyze reactions using O_2 as oxidant.

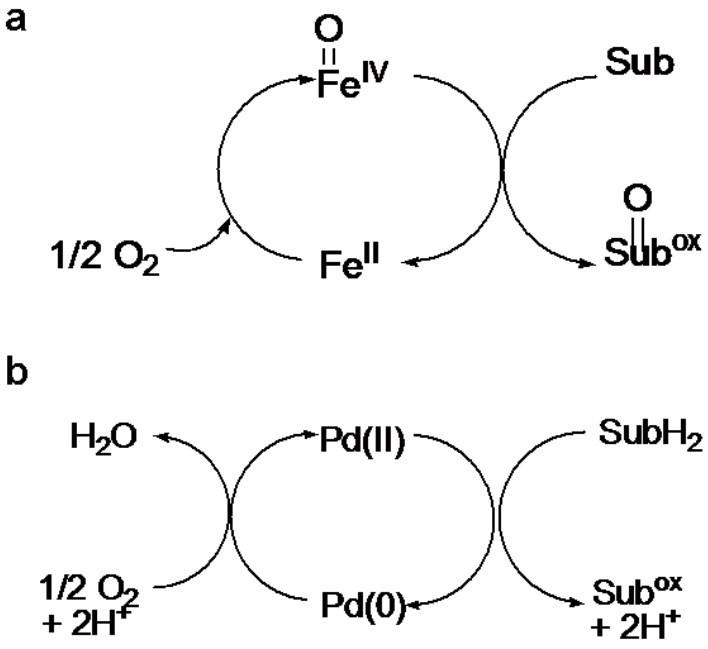

Figure 3.1 Catalytic cycle of (a). Fe in hemin catalyzed oxidation reactions using oxygen, where Fe undergoes two valence charge change (II to IV), and (b). Pd catalyzed oxidation reactions using oxygen, where Pd also undergoes two valence charge change (0 to II).

Heterogeneous nanoparticle catalysts are of increasing interest for long-term stability, recyclability and easer separation from the reaction mixture[79-82]. Molecular ligands play an essential role in the design of homogeneous molecular catalysts, where the molecular ligands can be used to tune the catalytic activity, selectivity, versatility and stability. The impact of molecular ligands on the tunability of nanoparticle catalysts is much less explored. Most efforts to date have been limited to the roles of molecular ligands in controlling size and facet of nanoparticles during nanoparticle synthetic steps. A few examples have suggested that a local ligand-induced microenvironment could enhance the catalytic activity by bringing catalyst and substrate into close proximity[83] or facilitate asymmetric reaction by chiral ligands[84]. Systematic ligand engineering studies are rarely reported towards nanoparticle catalysts simultaneously with enhanced catalytic activity and stability, especially for industrial relevant reactions. Here we report a systematic study of ligand effects on Pd nanoparticle catatlyst for phenol production from ketone under aerobic conditions.

Phenols are recognized as the key structure motif and core building block for a wide range of industrial chemicals[85]. The selective functionalization of phenols is generally challenging. The electrophilic substitution represents the most common methods for the synthesis of a variety of para- and ortho-substituted phenols, but is not applicable for meta-substituted phenols. Dehydrogenation of cyclohexanones followed by

tautomerization can result in meta-substituted phenols[86], but is often limited by relatively low conversion yield[87], harsh reaction conditions[88], poor functional group tolerance[89] and the requirement of additional sacrificial agents[90]. Stahl group has recently developed a homogeneous Pd^{II}-catalyzed dehydrogenation method to enable high yield dehydrogenative oxidation of 3-methylcyclohexenone to phenol in relatively mild reaction conditions using only oxygen as the oxidant[91]. However, the inevitable competition reaction of Pd deligation can result in large (> 100 nm), unreactive particles, leading to deactivation of catalytic activity[92,93]. Heterogenous Pd nanoparticles on different supports have been explored for dehydrogenation of cyclohexenones, but typically only extremely low yield (< 1.5%)[91].

Here we report a rational design and systematic investigation of the ligand effect on Pd nanoparticle catalysts for dehydrogenation of cyclohexenones, using butyric acid as capping ligands with variable γ-substitutions. Our studies show that the γ functional groups as a secondary binding site, can actively participate in the catalytic cycle to mediate the nanocatalyst activity and stability. Kinetic studies demonstrate that hydroxyl-substituted butyric acid can function as a particularly unique molecular ligand for Pd nanoparticles with excellent catalytic activity and stability, and can be used to catalyze the oxidation of 3-methylcyclohexenone to phenol with 93% yield and excellent recyclability. The Pd nanoparticles also have enhanced activity and stability than homogenous Pd(II) catalysts in high turnover conditions.

B. Nanoparticle synthesis and catalytic results

The dehydrogenative oxidation of 3-methylcyclohexenone to phenol involves dehydrogenation of cyclohexanones via sequential Pd-mediated C–H activation/β-hydride elimination steps, followed by tautomerization of dienone to produce phenol as the final product (Figure 3.2). It has been shown that homogeneous catalyst $Pd(TFA)_2$ could catalyze the reaction with moderate yield[91]. In the metal insertion and α-C-H activation step, acids are released and then re-enter the catalytic cycle via transmetallation step to regenerate catalytic active Pd(II) species. Acids are also released in the latter reductive elimination step. Introduction of additional acid like trifluoroacetic acid (TFA) could further increase the yield[91]. However, the inevitable competition reaction of Pd deligation can result in large (> 100 nm) inactive Pd nanoparticles, lowering the catalytic activity[92,93].

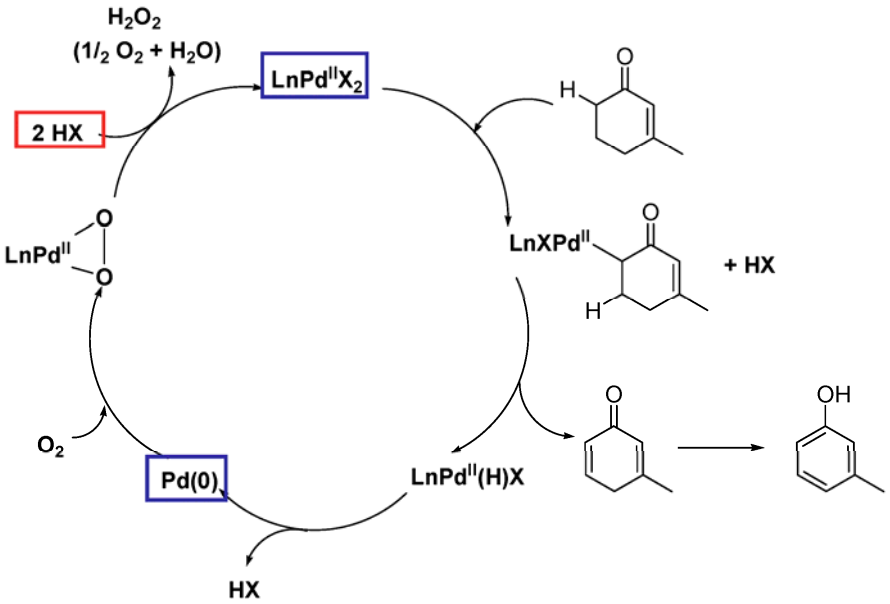

Figure 3.2 Catalytic mechanism of dehydrogenative oxidation of 3-methylcyclohexenone to phenol. 3-methylcyclohexenone undergoes dehydrogenation via sequential Pd-mediated C–H activation/β-hydride elimination steps, followed by tautomerization of the dienone intermediate to produce phenol.

The substitution of homogenous Pd catalysts with ultrafine Pd nanostructures can also catalyze the reaction, but requires additional acid activation. Our initial studies on commercial Pd/C showed nearly no activity without acid (yield <1%) (Table 3.1, Entry 1), consistent with previous studies[91]. The addition of weak acetic acid (HOAc) could slightly increase the yield (6%) (Table 3.1, Entry 2), while the introduction of a strong acid TFA could boost the yield to 67% (Table 3.1, Entry 3). However, the carbon black supported Pd nanoparticles can go through a serious Oswald ripening process to form large un-reactive particles (Fig. 3.3) with essentially no recyclability (yield <1% for the recycled Pd/C catalysts) (Table 3.1, Entry 4).

Table 3.1 Catalytic optimization of 3-methylcyclohexenone dehydrogenative oxidation.

Entry	Catalyst	Yield (%)*
1	Commercial Pd/C	<1
2	Commercial Pd/C, HOAc	6
3	Commercial Pd/C, TFA	67
4	Re-harvested commercial Pd/C, TFA	<1
5	HB-Pd/C, TFA	**93**
6	Re-harvested HB-Pd/C, TFA	**83**
7	AB-Pd/C, TFA	74
8	Re-harvested AB-Pd/C, TFA	24
9	CB-Pd/C, TFA	57
10	Re-harvested CB-Pd/C, TFA	48

*Reaction condition: 1 mmol 3-methylcyclohexenone, 0.03 mmol Pd equivalent catalyst, 100 ^{o}C under 1 atm oxygen for 24 h. The addition of acid is 1.2 mmol. Yield is obtained via GC-MS.

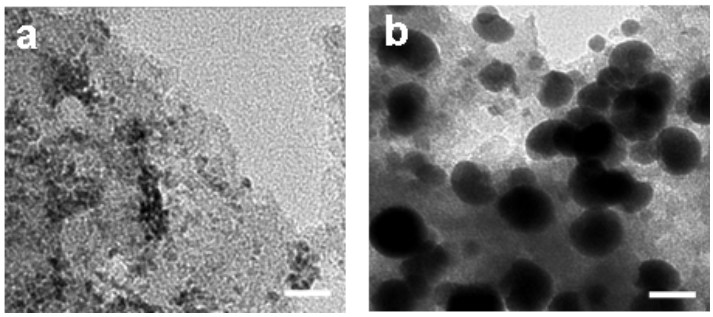

Figure 3.3 TEM morphology of commercial Pd/C (a). before reaction; (b). after 24 hr reaction. The scale bars are 40 nm.

The ripening issue of the commercial Pd/C could be attributed to the fact that Pd nanoparticles do not have proper ligand environment to protect them from leaching off Pd ions during the catalytic cycles. The use of ligands with strong binding functional group could ensure nanoparticle stability but often seriously compromise the catalytic activity due to the passivation of the catalytic active sites by the strong binding functional group[94]. Therefore, it is a significant challenge to design a proper surface ligand that can maintain particle stability without sacrificing the catalytic activity. To this end, we propose to use butyric acid with variable γ-substitution as secondary binding site to engineer the particle stability, instead of directly engineering the primary binding functional group, γ-functional groups as secondary binding site were engineered without direct passive the catalytic active sites. The γ-substituted butyric acids have been studied to exhibit many attractive attributes as a unique ligand for this purpose[95]. First, the ligand chain length of γ-substituted butyric acid provides necessary hydrophilicity−hydrophobicity balance for

maintaining particle size in aqueous solution synthesis. Second, side methyl group provide a confinement effect with proper ligand coverage on the particle surfaces to provide sufficient number of active catalytic centers. Third, γ-substituted functional group could offer secondary binding site to minimize leaching problems, subsidiary to primary carboxyl binding group during catalytic cycles.

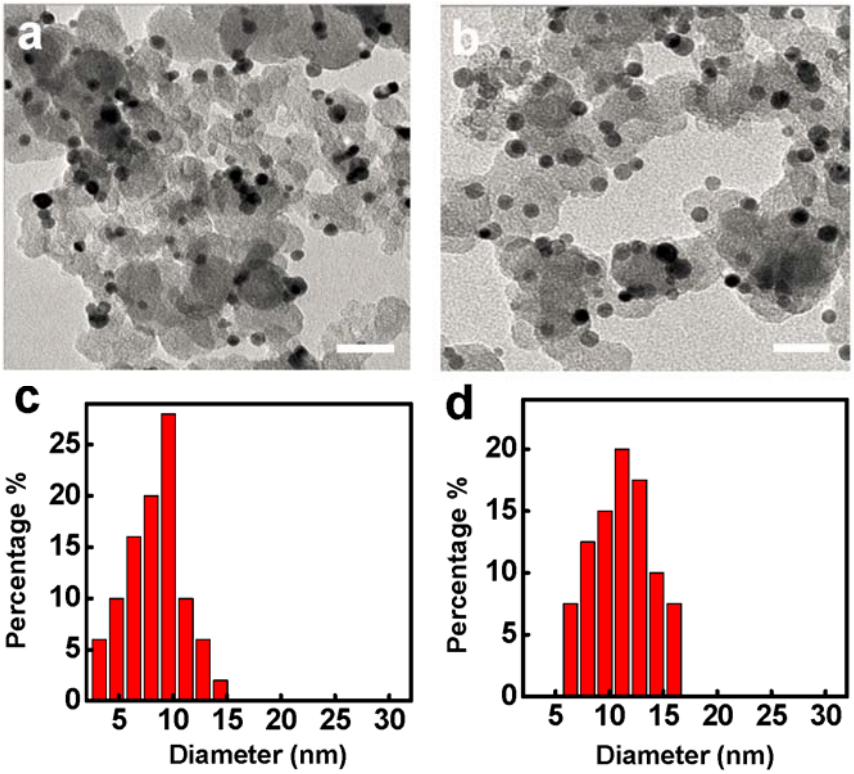

Figure 3.4 TEM morphology of HB-Pd/C (a). as synthesized; (b). after 24 hr reaction. The scale bars are 40 nm. Size distribution of HB-Pd/C (c). as synthesized; (d). after 24 hr reaction.

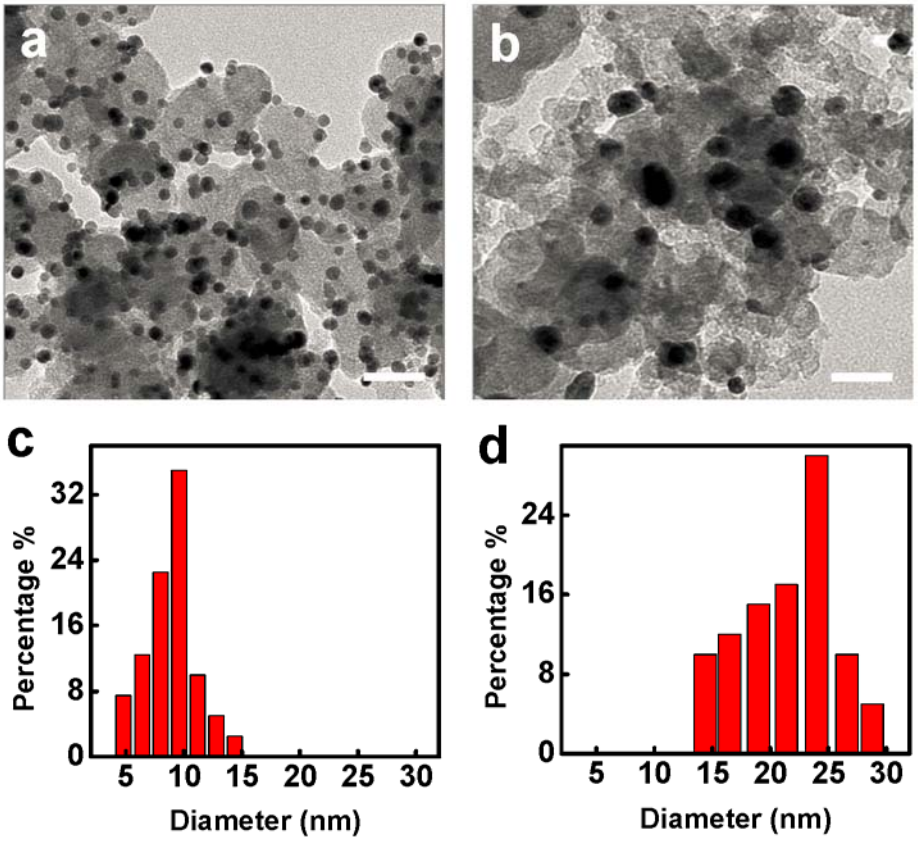

Figure 3.5 TEM morphology of AB-Pd/C (a). as synthesized; (b). after 24 hr reaction. The scale bars are 40 nm. Size distribution of AB-Pd/C (c). as synthesized; (d). after 24 hr reaction.

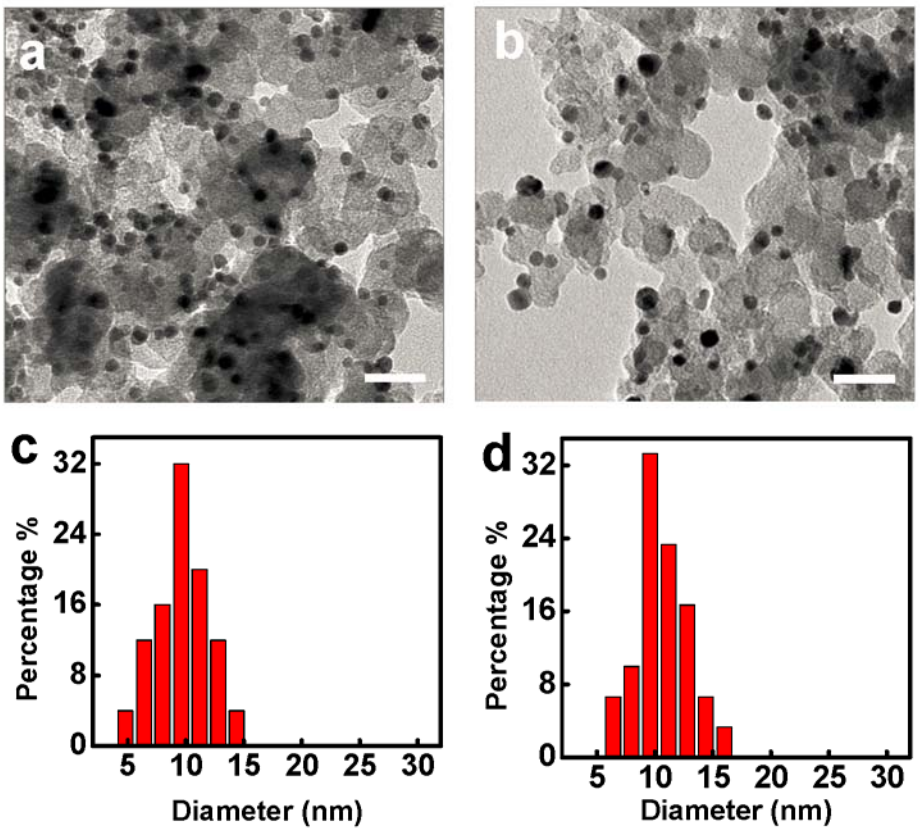

Figure 3.6 TEM morphology of CB-Pd/C (a). as synthesized; (b). after 24 hr reaction. The scale bars are 40 nm. Size distribution of CB-Pd/C (c). as synthesized; (d). after 24 hr reaction.

We have recently developed γ-substituted butyric acid as capping agent for the synthesis Pt nanoparticles[18]. Pd nanoparticles with 10 nm diameters were synthesized using a similar method with different γ-function groups (hydroxyl, amino, and choloro groups). The particle synthesis was done in aqueous solutions containing Na_2PdCl_4 as Pd precursor, ascorbic acid and $NaBH_4$ as reducing agent. These nanoparticles were then supported on carbon black for catalytic studies. The resulted carbon supported 3-hydroxylbutyric acid ligated Pd particles (HB-Pd/C), 3-aminobutyric acid ligated Pd

particles (AB-Pd/C) and 3-cholorobutyric acid ligated Pd particles (CB-Pd/C) all show an average size of ~10 nm (Fig. 3.4a,c; Fig. 3.5a,c; Fig 3.6a,c). The similarity in particle size over different ligands indicates that carboxyl group as the primary binding site dominates the binding affinity of the ligands to Pd(0) at particle surfaces, while γ-functional groups (hydroxyl, amino, and choloro) as secondary binding site don't significantly vary the binding conditions. FT-IR studies also further confirm the carboxyl group as the primary binding site (Fig 3.7).

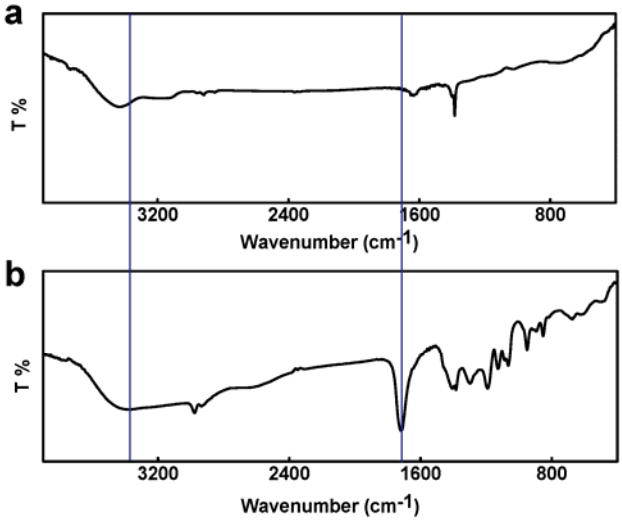

Figure 3.7 FT-IR spectrum of (a). HB-Pd/C. (b). HB. Compared to HB, ν(C=O) at around 1710 cm^{-1} disappeared and a new pair of peaks at around 1635 cm^{-1} showed up in the spectrum of HB-Pd. ν(-OH) also red shifted in HB-Pd, which indicated that γ-hydroxyl group of HB act as a secondary binding site to Pd.

We then investigate the catalytic behaviour of carbon supported Pd nanoparticles for aerobic dehydrogenative oxidation of cyclohexenones in TFA acidified conditions for 24 hours. The size of the Pd nanoparticles before and after catalyzing reaction was also investigated by TEM. Importantly, the catalytic studies show that HB-Pd/C catalyzed

reaction show a rather high yield up to 93% (Table 3.1), much higher than commercial Pd/C (Table 3.1). The reactions also demonstrate good heterogeneity by filtration test (Fig 3.8), consistent with the recent finding that 3-methylcyclohexenone dehydrogenative oxidation is catalyzed by heterogeneous Pd nanoparticles[15]. More importantly, after 24 hour reaction, the size of Pd nanoparticles doesn't show significant change (Fig. 3.4). This in stark contrast to commercial Pd/C catalysts, with a serious ripening process and increasing the in size (Fig. 3.3), and diminished catalytic active in reharvested material. With the size of the HB/Pd/C largely maintained during the catalytic cycle, the re-harvested HB-Pd/C exhibited nearly similar catalytic activity with a yield of 83% (Table 3.1). The small decrease in the reaction yield may be partly attributed to the incomplete re-harvest of all catalyst materials, and also probably attributed to the inevitable equilibrium amount of Pd(II) species present in the reaction solution due to the presence of Pd nanoparticles.

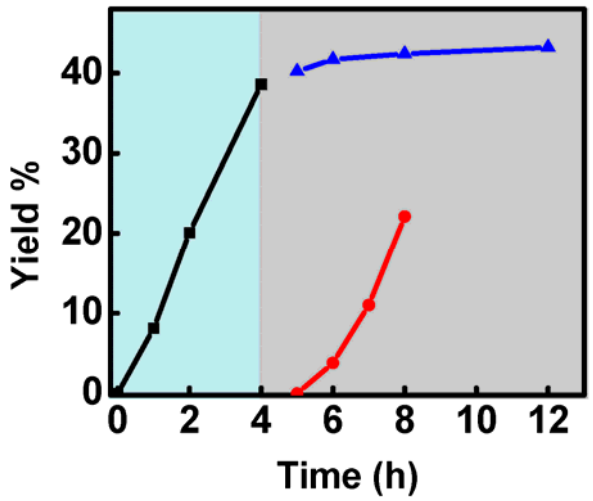

Figure 3.8 Filtration test of HB-Pd/C catalyzed reaction dehydrogenative oxidation reaction. HB-Pd/C catalyzed reaction was first allowed to run for 4 hours (black line), and then filtered. The supernatant was gathered back into reaction container and continue

reaction (blue line), while the filtered nanoparicles were washed and dispersed in new DMSO solution and react with reactant (red line). The results show that the supernatant exhibit nearly no reactivity, while the re-harvested catalysts could catalyze new reaction with nearly the same activity as the original reaction compared at the linear range. Filtration study clearly demonstrated that the reaction is dominated by heterogeneous HB-Pd/C, not homogeneous Pd species that leached into reaction solution.

We have tested the other two catalysts to further probe the effect of butyric acid ligand with different γ-functional groups. The yield of AB-Pd/C catalyzed reaction has a lower yield 74%, which reduces to 24% in reactions with the recycled AB-Pd/C (Table 3.1). The severe decrease of catalytic activity in the re-harvested catalyst may be attributed to obvious Oswald ripening the fact that AB-Pd nanoparticle during the catalytic cycle, with the average size increasing from ~10 nm to 20 nm after the first cycle of reaction (Fig. 3.5). The CB-Pd/C catalyzed reaction exhibits an even lower initial yield of 57% in its first cycle, which is however largely retained (48%) in the reharvested catalyst (Table 3.1). Overall, the HB-Pd/C shows the highest initial catalytic activity, together with excellent recyclability (with the catalytic activity of the recycled sample 2 times of CB-Pd/C and 3 times of AB-Pd/C catalysts). The average size of CB-Pd/C maintains the same after catalyzing reactions (Fig. 3.6).

Time dependant study also demonstrated that the maximum turnover frequency (TOF) of HB-Pd/C is around 4.33 h^{-1} per mol of Pd, high than commercial Pd/C (2.85 h^{-1} per mol of Pd), AB-Pd/C (2.03 h^{-1} per mol of Pd) and HB-Pd/C (1.48 h^{-1} per mol of Pd). The reaction kinetics of re-harvested HB-Pd/C (Fig. 3.9a) and AB-Pd/C (Fig. 3.9c)

largely retained their catalytic activity, which AB-Pd/C lost nearly 70% of its catalytic activity (Fig. 3.9b) and commercial Pd/C essentially lost all of its activity.

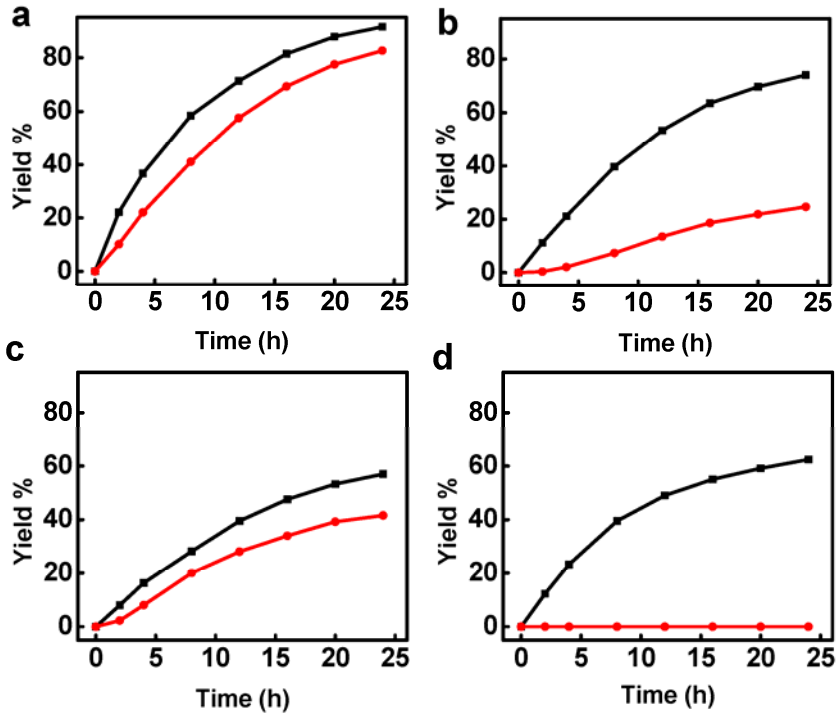

Figure 3.9 Time dependant study of 3-methylcyclohexenone dehydrogenative oxidation. Time dependant reaction catalyzed by (a). HB-Pd/C, (b). AB-Pd/C, (c). CB-Pd/C (blue line) and (d). commercial Pd/C. Black lines represent the catalytic studies of fresh catalysts, red lines represent the catalytic studies of re-harvested catalysts.

C. Investigation of ligand effect

To further study the effect of Oswald ripening on the activity and recyclability of different ligand capped nanoparticle catalysts, the catalytic cycle and binding strength of the ligands to Pd(II) is further investigated. Pd(0) sites on the particle surface have to be activated to Pd(II) by oxygen and acid, to catalyze the following transformation. However, the amount of leached-out Pd(II) from the particle surfaces would

predominately lead to the Oswald ripening effect. The use of strong binding ligand on particle surface to Pd(II) is a possible method to concur the leaching- out problem, but would sacrifice catalytic activity. As a result, the proper binding strength of ligands on the surface to Pd(II) would play an essential role to maintain the catalytic activity as well as stability. Predicted by Hard-soft acid base theory (HSABT)[97], the binding strength to Pd(II) is Cl > N > O. Cl has the strongest binding strength to prevent Pd(II) from leaching-out from the surface, so that CB-Pd/C has the best recyclability. XPS studies show there is significant more proportion of Pd(II) than Pd(0) after reaction than as synthesized (Fig. 3.10), indicating a large portion of Pd is activated to Pd(II) and stabilized on the particle surface. On the other hand, the reactivity is greatly passivated also due to the tight binding of 3-cholorobutyric acid to Pd(II). The low catalytic activity of CB-Pd/C could also be attributed to the fact that halide ligand could inhibit β-H elimination step to yield dienone product which could undergo tautomerization to phenol, and rather favor protonolysis which could result in regeneration of the substrate or/and blocking catalytic sites[98-100]. AB-Pd/C has the most obvious Oswald ripening seems contradictory to the prediction. To understand this fact, zeta potential measurements were preformed. Zeta potentials of Pd particles with different ligands were measured before and after dispersing into reaction solution, namely, DMSO solution containing TFA. All particles show a positive shift of zeta potential after dispersing into TFA/DMSO solution and washing process. This is attributed to the partial protonation of the carboxyl group of all the three ligands by TFA. HB-Pd and CB-Pd still remain negative after this process. On the contrary, AB-Pd shift from negative to positive, which can be attributed to the additional protonation of amine group to form positively charged NH_3^+, which lost almost

all the binding affinity to Pd(II). Moreover, those activated Pd(II) sites could more likely be pushed away from AB-Pd surface due to electron repulsion than electron attraction force in HB-Pd and CB-Pd. This process could greatly accelerate Oswald ripening of Pd nanoparticles which resulted in low catalytic activity and poor recyclability.

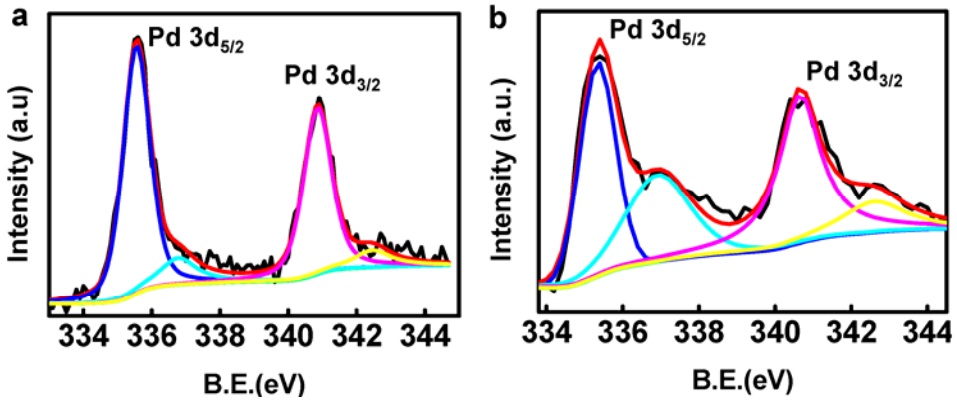

Figure 3.10 XPS spectra of CB-Pd/C before and after reaction in Pd 3d region. (a). as synthesized, (b). harvested after catalyzing reaction. Blue lines and pink lines are the simulated results for Pd(0) for Pd $3d_{5/2}$ and Pd $3d_{3/2}$. Green lines and yellow lines are the simulated results for Pd(II) for Pd $3d_{5/2}$ and Pd $3d_{3/2}$. The peak intensities of Pd(II) are much higher compared to Pd(0) after reaction.

Table 3.2 Zeta potential measurements of Pd nanoparticles before and after dispersing into TFA/DMSO solution for 24 hours.

Entry	Catalyst	Zeta potential (mV)
1	HB-Pd, before	-23.2
2	HB-Pd, after	-2.79
3	CB-Pd, before	-21.6
4	CB-Pd, after	-3.76

5	AB-Pd, before	-18.4
6	AB-Pd, after	**2.41**

D. Comparison studies between heterogeneous and homogeneous catalysts

We then compare the catalytic behavior of the best heterogeneous catalyst HB-Pd/C with homogeneous catalyst $Pd(TFA)_2$ (Fig. 3.11). In low turnover conditions, namely low substrate:catalyst ratio (100:3), the turnover number (TON) of HB-Pd/C (31 per mol of Pd) is 1.5 times higher than $Pd(TFA)_2$ (20 per mol of Pd) after a 24-h reaction. HB-Pd/C also has a better maximum TOF (around 4.33 h^{-1} per mol of Pd) then $Pd(TFA)_2$ (around 2.34 h^{-1} per mol of Pd). A significant drawback of homogeneous catalyst is the competition deligation reaction to form large unreactive Pd black. This competition reaction is greatly accelerated under conditions of high substrate:catalyst ratio[101-103], which inevitably limit the potential applications of homogeneous catalysts in high turnover conditions. The reactions under high substrate;catalyst ratio (1000:3) exhibit a completely different behavior. HB-Pd/C could drive the reaction to almost completion for a 120-h test period (yield 95.4%). The TON reaches 318 per mol of Pd, ten times higher than the reaction in low turnover conditions, proving the retained catalytic activity of HB-Pd/C. While $Pd(TFA)_2$ could only produce a small amount of the product, resulted in the TON of 28 per mol of Pd, only slightly higher than the TON in low substrate:catalyst ratio condition (20 per mol of Pd). The loss of catalytic activity of $Pd(TFA)_2$ is due to the fact that large unreactive Pd black particles form after the reaction initialized (Fig. 3.12) and precipitate out from the reaction solution.

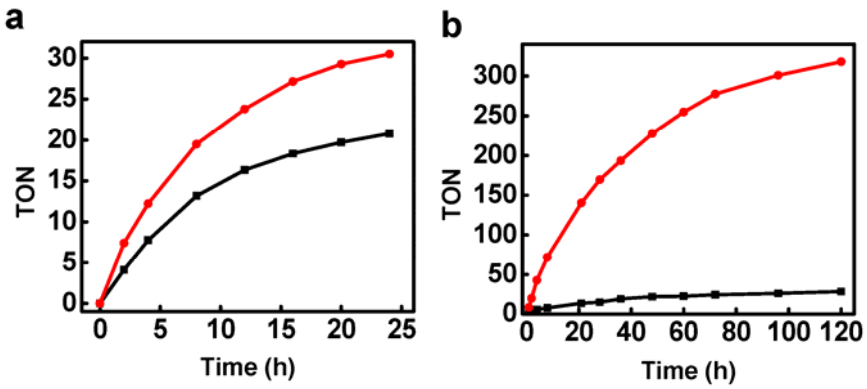

Figure 3.11 Time dependant study of 3-methylcyclohexenone dehydrogenative oxidation with different substrate:catalyst ratio. TON of time dependant reaction catalyzed by HB-Pd/C (red line) and $Pd(TFA)_2$ (black line) with substrate:catalyst ratio of (a). 100:3, (b). 1000:3.

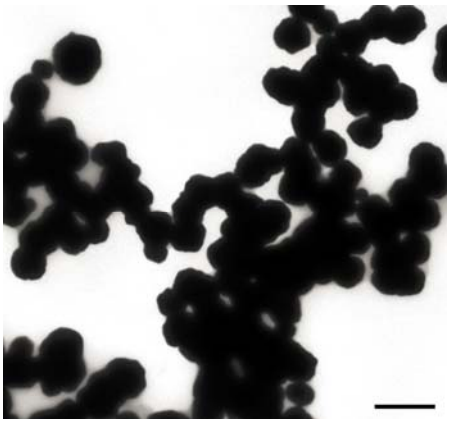

Figure 3.12 TEM image of large particle formation after homogeneous $Pd(TFA)_2$ catalyzed reaction. The scale bar is 500 nm.

E. Discussion and conclusion

By systematically engineering the ligands on the surface of Pd nanoparticle catalysts, we have accomplished heterogeneous catalyzed dehydrogenative oxidation of ketone to phenol with high yield and good recyclability simultaneously. Further in-depth studies revealed that γ-substitution group plays a significant roll for the high efficiency

and robust characteristic of Pd nanoparticle catalysts by mediating catalytic cycle. Overall, our studies demonstrate a strategy to convert homogeneous catalyzed reaction to heterogeneous, and enable important chemical transformations not otherwise readily possible. It can impact diverse areas including synthetic methodology and green chemistry.

Conclusion

Three biomimetic catalysts have been studied detailed above.

The immobilization of monomeric hemin on graphene can form stable conjugates. Graphene-hemin conjugates demonstrate excellent catalytic activity, over 10 times better than that of the recently developed hemin-hydrogel system and 100 times better than that of unsupported hemin. The catalysts also exhibit excellent binding affinity and catalytic efficiency approaching that of natural enzymes. Graphene-hemin conjugates are used to facilitate nitric oxide generation with a catalytic activity much higher than resin-supported system.

We designed a novel graphene-hemin-glucose oxidase (GOx) conjugate as a tandem catalyst, in which graphene functions as a unique support to integrate molecular catalyst hemin and enzymetic catalyst GOx with retained functionality for biomimetic generation of antithrombotic species. We show that the monomeric hemin can be conjugated with graphene through π-π interactions to function as an effective catalyst for the oxidation of endogenous L-arginine by H_2O_2. Furthermore, we show that GOx can be covalently linked onto graphene for local generation of H_2O_2 through the oxidation of blood glucose. Thus, the integrated graphene-hemin-GOx catalysts can readily enable the continuous generation of nitroxyl, an antithrombotic species, from physiologically abundant glucose and L-arginine. We demonstrate the conjugates can be embedded within polyurethane to create a novel, long-lasting antithrombotic coating for blood contacting biomedical devices.

We did a systematic investigation of γ-substituted butyric acid ligands for the creation of a highly robust and efficient Pd nanoparticle heterogeneous catalysts for a novel aerobic phenol production reaction. By varying the γ-substitution, yield was optimized to 93 %, much higher than 1.5 % reported previously, exhibiting good heterogeneity and recyclability. Systematic mechanistic studies demonstrate that the γ-functional groups can significantly impact on the reaction pathway to modify the catalytic activity and stability. The resulted heterogeneous catalysts also present also have far better activity and stability than homogenous Pd(II) catalysts in high turnover conditions. This work could open up new insight for the design and engineer of molecular ligands for heterogeneous catalysts.

Refenerces

1. Genfa, Z. & Dasgupta, P. K. Hematin as a peroxidase substitute in hydrogen peroxide determinations. *Analytical Chemistry* **64**, 517-522 (1992).

2. Bruice, T. C. Reactions of hydroperoxides with metallotetraphenylporphyrins in aqueous-solutions. *Accounts of Chemical Research* **24**, 243-249 (1991).

3. Mansuy, D. Activation of alkanes – the biomimetic approach. *Coordination Chemistry Reviews* **125**, 129-141 (1993).

4. Shema-Mizrachi, M., Pavan, G. M., Levin, E., Danani, A. & Lemcoff, N. G. Catalytic chameleon dentrimers. *Journal of the American Chemical Society*, **133**, 14359-14367, doi:10.1021/ja203690k (2011).

5. Bedioui, F. Zeolite-encapsulated and clay-intercalated metal porphyrin, phthalocyanine and Schiff-base complexes as models for biomimetic oxidation catalysis – an overiew. *Coordination Chemistry Reviews* **144**, 39-68 (1995).

6. Wang, Q. G. *et al.* A supramolecular-hydrogel-encapsulated hemin as an artificial enzyme to mimic peroxidase. *Angew. Chem.-Int. Edit.* **46**, 4285-4289, doi:10.1002/anie.200700404 (2007).

7. Wang, Q., Yang, Z., Ma, M., Chang, C. K. & Xu, B. High catalytic activities of artificial peroxidases based on supramolecular hydrogels that contain heme models. *Chemistry-a European Journal* **14**, 5073-5078, doi:10.1002/chem.200702010 (2008).

8. Yamaguchi, H., Tsubouchi, K., Kawaguchi, K., Horita, E. & Harada, A. Peroxidase activity of cationic metalloporphyrin-antibody complexes. *Chemistry-a European Journal* **10**, 6179-6186, doi:10.1002/chem.200305692 (2004).

9. Mukherjee, M. & Ray, A. R. Biomimetic oxidation of L-arginine with hydrogen peroxide catalyzed by the resin-supported iron (III) porphyrin. *Journal of Molecular Catalysis a-Chemical* **266**, 207-214, doi:10.1016/j.molcata.2006.11.012 (2007).

10. Geim, A. K. & Novoselov, K. S. The rise of graphene. *Nature Materials* **6**, 183-191, doi:10.1038/nmat1849 (2007).

11. Schwierz, F. Graphene transistors. *Nature Nanotechnology* **5**, 487-496, doi:10.1038/nnano.2010.89 (2010).

12. Bai, J. *et al.* Very large magnetoresistance in graphene nanoribbons. *Nature Nanotechnology* **5**, 655-659, doi:10.1038/nnano.2010.154 (2010).

13. Liao, L. *et al.* High-speed graphene transistors with a self-aligned nanowire gate. *Nature* **467**, 305-308, doi:10.1038/nature09405 (2010).

14. Park, S. & Ruoff, R. S. Chemical methods for the production of graphenes. *Nature Nanotechnology* **4**, 217-224, doi:10.1038/nnano.2009.58 (2009).

15. Allen, M. J., Tung, V. C. & Kaner, R. B. Honeycomb Carbon: A Review of Graphene. *Chemical Reviews* **110**, 132-145, doi:10.1021/cr900070d (2010).

16. Jiao, L., Zhang, L., Wang, X., Diankov, G. & Dai, H. Narrow graphene nanoribbons from carbon nanotubes. *Nature* **458**, 877-880, doi:10.1038/nature07919 (2009).

17. Stankovich, S. *et al.* Synthesis of graphene-based nanosheets via chemical reduction of exfoliated graphite oxide. *Carbon* **45**, 1558-1565, doi:10.1016/j.carbon.2007.02.034 (2007).

18. Li, D., Mueller, M. B., Gilje, S., Kaner, R. B. & Wallace, G. G. Processable aqueous dispersions of graphene nanosheets. *Nature Nanotechnology* **3**, 101-105, doi:10.1038/nnano.2007.451 (2008).

19. Tung, V. C., Allen, M. J., Yang, Y. & Kaner, R. B. High-throughput solution processing of large-scale graphene. *Nature Nanotechnology* **4**, 25-29, doi:10.1038/nnano.2008.329 (2009).

20. Dai, B. Y. *et al.* High-Quality Single-Layer Graphene via Reparative Reduction of Graphene Oxide. *Nano Research* **4**, 434-439, doi:10.1007/s12274-011-0099-8 (2011).

21. Tung, V. C. *et al.* Surfactant-Free Water-Processable Photoconductive All-Carbon Composite. *Journal of the American Chemical Society* **133**, 4940-4947, doi:10.1021/ja1103734 (2011).

22. Liang, Y. *et al.* Co_3O_4 nanocrystals on graphene as a synergistic catalyst for oxygen reduction reaction. *Nature Materials* **10**, 780-786, doi: 10.1038/nmat3087 (2011).

23. Xu, Y. *et al.* Chemically converted graphene induced molecular flattening of 5,10,15,20-tetrakis(1-methyl-4-pyridinio)porphyrin and its application for optical detection of cadmium(II) ions. *Journal of the American Chemical Society* **131**, 13490-13497, doi:10.1021/ja905032g (2009).

24. Geng, J. & Jung, H.-T. Porphyrin functionalized graphene sheets in aqueous suspensions: from the preparation of graphene sheets to highly conductive graphene films. *Journal of Physical Chemistry C* **114**, 8227-8234, doi:10.1021/jp1008779 (2010).

25. Ghosh, A., Rao, K. V., George, S. J. & Rao, C. N. R. Noncovalent functionalization, Exfoliation, and solubilization of graphene in water by employing a fluorescent coronene carboxylate. *Chemistry-a European Journal* **16**, 2700-2704, doi:10.1002/chem.200902828 (2010).

26. Chen, J., Zhao, L., Bai, H. & Shi, G. Electrochemical detection of dioxygen and hydrogen peroxide by hemin immobilized on chemically converted graphene. *Journal of Electroanalytical Chemistry* **657**, 34-38, doi:10.1016/j.jelechem.2011.03.005 (2011).

27. Zhang, S., Tang, S., Lei, J., Dong, H. & Ju, H. Functionalization of graphene nanoribbons with porphyrin for electrocatalysis and amperometric biosensing. *Journal of Electroanalytical Chemistry* **656**, 285-288, doi:10.1016/j.jelechem.2010.10.005 (2011).

28. Guo, C. X., Lei, Y. & Li, C. M. Porphyrin functionalized graphene for sensitive electrochemical detection of ultratrace explosives. *Electroanalysis* **23**, 885-893, doi:10.1002/elan.201000522 (2011).

29. Guo, Y. *et al.* Hemin-graphene hybrid nanosheets with intrinsic peroxidase-like activity for label-free colorimetric detection of single-nucleotide polymorphism. *Acs Nano* **5**, 1282-1290, doi:10.1021/nn1029586 (2011).

30. Hummers, W. S. & Offeman, R. E. Preparation of graphitic oxide. *Journal of the American Chemical Society* **80**, 1339-1339, doi:10.1021/ja01539a017 (1958).

31. Ryabova, E. S. *et al.* Preparation and reactivity studies of synthetic microperoxidases containing b-type heme. *Journal of Biological Inorganic Chemistry* **9**, 385-395, doi:10.1007/s00775-004-0532-5 (2004).

32. Smulevich, G. *et al.* Effect of the His175 – Glu mutation on the heme pocket architecture of Cytochrome-c peroxidase. *Biochemistry* **34**, 13485-13490, doi:10.1021/bi00041a028 (1995).

33. Silver, J. & Lukas, B. Mossbauer studies on protoporphyrin-IX iron(III) solutions. *Inorganica Chimica Acta-Bioinorganic Chemistry* **78**, 219-224, doi:10.1016/s0020-1693(00)86516-0 (1983).

34. Ullrich, V. Thoughts on thiolate tethering. Tribute and thanks to a teacher. *Archives of Biochemistry and Biophysics* **409**, 45-51, doi:Pii s0003-9861(02)00410-1 10.1016/s0003-9861(02)00410-1 (2003).

35. Moreira, M. S. M., Martins, P. R., Curi, R. B., Nascimento, O. R. & Iamamoto, Y. Iron porphyrins immobilised on silica surface and encapsulated in silica matrix: a comparison of their catalytic activity in hydrocarbon oxidation. *Journal of Molecular Catalysis a-Chemical* **233**, 73-81, doi:10.1016/j.molcata.2005.01.045 (2005).

36. Feiters, M. C., Rowan, A. E. & Nolte, R. J. M. From simple to supramolecular cytochrome P450 mimics. *Chemical Society Reviews* **29**, 375-384, doi:10.1039/a804252g (2000).

37. Szacilowski, K., Chmura, A. & Stasicka, Z. Interplay between iron complexes, nitric oxide and sulfur ligands: Structure, (photo)reactivity and biological importance. *Coordination Chemistry Reviews* **249**, 2408-2436, doi:10.1016/j.ccr.2005.03.021 (2005).

38. Harris, D., Loew, G. & Waskell, L. Structure and spectra of ferrous dioxygen and reduced ferrous dioxygen model cytochrome P450. *Journal of the American Chemical Society* **120**, 4308-4318, doi:10.1021/ja974110q (1998).

39. Walker, F. A. Nitric oxide interaction with insect nitrophorins and thoughts on the electron configuration of the {FeNO}(6) complex. *Journal of Inorganic Biochemistry* **99**, 216-236, doi:10.1016/j.jinorgbio.2004.10.009 (2005).

40. Weichsel, A. *et al.* Heme-assisted S-nitrosation of a proximal thiolate in a nitric oxide transport protein. *Proceedings of the National Academy of Sciences of the United States of America* **102**, 594-599, doi:10.1073/pnas.0406549102 (2005).

41. Fiedler, D., Leung, D. H., Bergman, R. G. & Raymond, K. N. Selective molecular recognition, C-H bond activation, and catalysis in nanoscale reaction vessels. *Accounts of Chemical Research* **38**, 349-358, doi:10.1021/ar040152p (2005).

42. Breslow, R. & Overman, L. E. "Artificial enzyme" combining a metal catalytic group and a hydrophobic binding cavity. *Journal of the American Chemical Society* **92**, 1075-1077, doi:10.1021/ja00707a062 (1970).

43. Hailes, H. C., Dalby, P. A. & Woodley, J. M. Integration of biocatalytic conversions into chemical syntheses. *Journal of Chemical Technology and Biotechnology* **82**, 1063-1066, doi:10.1002/jctb.1763 (2007).

44. Marr, A. C. & Liu, S. Combining bio- and chemo-catalysis: from enzymes to cells, from petroleum to biomass. *Trends in Biotechnology* **29**, 199-204, doi:10.1016/j.tibtech.2011.01.005 (2011).

45. Krumlinde, P., Bogar, K. & Backvall, J.-E. Asymmetric synthesis of bicyclic diol derivatives through metal and enzyme catalysis: application to the formal synthesis of sertraline. *Chemistry-a European Journal* **16**, 4031-4036, doi:10.1002/chem.200903114 (2010).

46. Deska, J., Ochoa, C. d. P. & Backvall, J.-E. Chemoenzymatic dynamic kinetic resolution of axially chiral allenes. *Chemistry-a European Journal* **16**, 4447-4451, doi:10.1002/chem.201000301 (2010).

47. Wang, Z. J., Clary, K. N., Bergman, R. G., Raymond, K. N. & Toste, F. D. A supramolecular approach to combining enzymatic and transition metal catalysis. *Nat Chem* **5**, 100-103,

doi:http://www.nature.com/nchem/journal/v5/n2/abs/nchem.1531.html#supplementary-information (2013).

48. Dwyer, A. Surface-treated catheters-a review. *Seminars in Dialysis* **21**, 542-546, doi:10.1111/j.1525-139X.2008.00499.x (2008).

49. Radomski, M. W., Palmer, R. M. J. & Moncada, S. The role of nitric-oxide and cGMP in platelet-adhesion to vascular endothelium. *Biochemical and Biophysical Research Communications* **148**, 1482-1489, doi:10.1016/s0006-291x(87)80299-1 (1987).

50. Vaughn, M. W., Kuo, L. & Liao, J. C. Estimation of nitric oxide production and reaction rates in tissue by use of a mathematical model. *American Journal of Physiology-Heart and Circulatory Physiology* **274**, H2163-H2176 (1998).

51. Keefer, L. K. Progress toward clinical application of the nitric oxide-releasing diazeniumdiolates. *Annual Review of Pharmacology and Toxicology* **43**, 585-607, doi:10.1146/annurev.pharmtox.43.100901.135831 (2003)

52. Frost, M. C., Reynolds, M. M. & Meyerhoff, M. E. Polymers incorporating nitric oxide releasing/generating substances for improved biocompatibility of blood-contactincy medical devices. *Biomaterials* **26**, 1685-1693, doi:10.1016/j.biomaterials.2004.06.006 (2005).

53. Major, T. C. et al. The attenuation of platelet and monocyte activation in a rabbit model of extracorporeal circulation by a nitric oxide releasing polymer. *Biomaterials* **31**, 2736-2745, doi:10.1016/j.biomaterials.2009.12.028 (2010).

54. Yan, Q., Major, T. C., Bartlett, R. H. & Meyerhoff, M. E. Intravascular glucose/lactate sensors prepared with nitric oxide releasing poly(lactide-co-glycolide)-

based coatings for enhanced biocompatibility. *Biosensors & Bioelectronics* **26**, doi:10.1016/j.bios.2011.04.026 (2011).

55. Parzuchowski, P. G., Frost, M. C. & Meyerhoff, M. E. Synthesis and characterization of polymethacrylate-based nitric oxide donors. *Journal of the American Chemical Society* **124**, 12182-12191, doi:10.1021/ja020268l (2002).

56. Kroencke, K. D. & Suschek, C. V. Adulterated effects of nitric oxide - generating donors. *Journal of Investigative Dermatology* **128**, 258-260, doi:10.1038/sj.jid.5701162 (2008).

57. Hwang, S. & Meyerhoff, M. E. Polyurethane with tethered copper(II)-cyclen complex: preparation, characterization and catalytic generation of nitric oxide from S-nitrosothiols. *Biomaterials* **29**, 2443-2452, doi:10.1016/j.biomaterials.2008.02.004 (2008).

58. Cha, W. & Meyerhoff, M. E. Catalytic generation of nitric oxide from S-nitrosothiols using immobilized organoselenium species. *Biomaterials* **28**, 19-27, doi:10.1016/j.biomaterials.2006.08.019 (2007).

59. Giustarini, D., Milzani, A., Dalle-Donne, I. & Rossi, R. Detection of S-nitrosothiols in biological fluids: A comparison among the most widely applied methodologies. *Journal of Chromatography B-Analytical Technologies in the Biomedical and Life Sciences* **851**, 124-139, doi:10.1016/j.jchromb.2006.09.031 (2007).

60. Mugesh, G., du Mont, W. W. & Sies, H. Chemistry of biologically important synthetic organoselenium compounds. *Chemical Reviews* **101**, 2125-2179, doi:10.1021/cr000426w (2001).

61. Cai, W., Wu, J., Xi, C., Ashe, A. J., III & Meyerhoff, M. E. Carboxyl-ebselen-based layer-by-layer films as potential antithrombotic and antimicrobial coatings. *Biomaterials* **32**, 7774-7784, doi:10.1016/j.biomaterials.2011.06.075 (2011).

62. Marletta, M. A. Nitric-oxide synthase – aspects concerning structure and catalysis. *Cell* **78**, 927-930, doi:10.1016/0092-8674(94)90268-2 (1994).

63. Nathan, C. & Xie, Q. W. Nitric-oxide synthases – roles, tolls, and controls. *Cell* **78**, 915-918, doi:10.1016/0092-8674(94)90266-6 (1994).

64. Fukuto, J. M., Dutton, A. S. & Houk, K. N. The chemistry and biology of nitroxyl (HNO): A chemically unique species with novel and important biological activity. *Chembiochem* **6**, 612-619, doi:10.1002/cbic.200400271 (2005).

65. Bermejo, E. et al. Effect of nitroxyl on human platelets function. *Thrombosis and Haemostasis* **94**, 578-584, doi:10.1160/th05-01-0062 (2005).

66. Pufahl, R. A., Wishnok, J. S. & Marletta, M. A. Hydrogen peroxide-supported oxidation of N^G-hydroxy-L-arginine by nitric oxide synthases. *Biochemistry* **34**, 1930-1941, doi:10.1021/bi00006a014 (1995)

67. Mukherjee, M. & Ray, A. R. Nitric oxide synthase-like activity of ion exchange resins modified with iron (III) porphyrins in the oxidation of L-arginine by H_2O_2: Mechanistic insights. *Catalysis Communications* **8**, 1431-1437, doi:10.1016/j.catcom.2006.12.010 (2007).

68. Haber, J., Mlodnicka, T. & Poltowicz, J. Metal-dependent reactivity of some metalloporphyrins in oxidation with dioxygen. *Journal of Molecular Catalysis* **54**, 451-461, doi:10.1016/0304-5102(89)80160-9 (1989).

69. Mukherjee, M. & Ray, A. R. Biomimetic oxidation of L-arginine with hydrogen peroxide catalyzed by the resin-supported iron (III) porphyrin. *Journal of Molecular Catalysis a-Chemical* **266**, 207-214, doi:10.1016/j.molcata.2006.11.012 (2007).

70. Xue, T. et al. Graphene-supported hemin as a highly active biomimetic oxidation catalyst. *Angewandte Chemie-International Edition* **51**, 3822-3825, doi:10.1002/anie.201108400 (2012).

71. Guo, Y. *et al.* Hemin-graphene hybrid nanosheets with intrinsic peroxidase-like activity for label-free colorimetric detection of single-nucleotide polymorphism. *Acs Nano* **5**, 1282-1290, doi:10.1021/nn1029586 (2011).

72. Peng, B. & Meyerhoff, M. E. Reexamination of the Direct Electrochemical Reduction of S-Nitrosothiols. *Electroanalysis* **25**, 914-921, doi:10.1002/elan.201200445 (2013).

73. Donzelli, S. *et al.* Generation of nitroxyl by heme protein-mediated peroxidation of hydroxylamine but not N-hydroxy-L-arginine. *Free Radical Biology and Medicine* **45**, 578-584, doi:10.1016/j.freeradbiomed.2008.04.036 (2008).

74. Kasper, H. *et al.* Urinary amino acid analysis: A comparison of iTRAQ®- LC-MS/MS, GC-MS, and amino acid analyzer. *Journal of Chromatography B,* **877**, 1838-1846, doi: 10.1016/j.jchromb.2009.05.019 (2009).

75. Espey, M. G., Miranda, K. M., Thomas, D. D. & Wink, D. A. Ingress and reactive chemistry of nitroxyl-derived species within human cells. *Free Radical Biology and Medicine* **33**, 827-834, doi:10.1016/s0891-5849(02)00978-4 (2002).

76. Chance, B., Sies. H. & Boveris A. Hydroperoxide metabolism in mammalian organs. *Physiol Rev* **59**, 527-605 (1979).

77. Liu, Y., Yu, D., Zeng, C., Miao, Z. & Dai, L. Biocompatible graphene oxide-based glucose biosensors. *Langmuir* **26**, 6158-6160, doi:10.1021/la100886x (2010).

78. Wu, Y., Zhou, Z. & Meyerhoff, M. E. *In vitro* platelet adhesion on polymeric surfaces with varying fluxes of continuous nitric oxide release. *Journal of Biomedical Materials Research Part A* **81A**, 956-963, doi:10.1002/jbm.a.31105 (2007).

79. Li, Y. *et al.* A Pt-cluster-based heterogeneous catalyst for homogeneous catalytic reactions: X-ray absorption spectroscopy and reaction kinetic studies of their activity and Stability against Leaching. *Journal of the American Chemical Society* **133**, 13527-13533, (2011).

80. Witham, C. A. *et al.* Converting homogeneous to heterogeneous in electrophilic catalysis using monodisperse metal nanoparticles. *Nature Chemistry* **2**, 36-41, (2010).

81. Reimann, S. *et al.* Identification of the active species generated from supported Pd catalysts in Heck Reactions: an in situ quick scanning EXAFS Investigation. *Journal of the American Chemical Society* **133**, 3921-3930, (2011).

82. Pachon, L. D. & Rothenberg, G. Transition-metal nanoparticles: synthesis, stability and the leaching issue. *Applied Organometallic Chemistry* **22**, 288-299, (2008).

83. Zaramella, D., Scrimin, P. & Prins, L. J. Self-assembly of a catalytic multivalent peptide-nanoparticle complex. *Journal of the American Chemical Society* **134**, 8396-8399, (2012).

84. Tamura, M. & Fujihara, H. Chiral bisphosphine BINAP-stabilized gold and palladium nanoparticles with small size and their palladium nanoparticle-catalyzed asymmetric reaction. *Journal of the American Chemical Society* **125**, 15742-15743, (2003).

85. Tyman, J. H. P. *Synthetic and Natural Phenols* (Elsevier, New York, 1996)

86. Gligorich, K. M. & Sigman, M. S. Recent advancements and challenges of palladium(II)-catalyzed oxidation reactions with molecular oxygen as the sole oxidant. *Chemical Communications*, 3854-3867, (2009).

87. Yi, C. S. & Lee, D. W. Efficient dehydrogenation of amines and carbonyl compounds catalyzed by a tetranuclear ruthenium-mu-oxo-mu-hydroxo-hydride complex. *Organometallics* **28**, 947-949, (2009).

88. Muzart, J. & Pete, J. P. Dehydrogenation of cyclohexanones catalyzed by palladium (II) trifluoroacetate. *Journal of Molecular Catalysis* **15**, 373-376, (1982).

89. Muzart, J. One-pot syntheses of alpha,beta-unsaturated carbonyl compounds through palladium-mediated dehydrogenation of ketones, aldehydes, esters, lactones and amides. *European Journal of Organic Chemistry*, 3779-3790, (2010).

90. Buckle, D. R. in *Encyclopedia of Reagents for Organic Synthesis*, D. Crich, Ed. (Wiley, New York, 2010).

91. Izawa, Y., Pun, D. & Stahl, S. S. Palladium-catalyzed aerobic dehydrogenation of substituted cyclohexanones to phenols. *Science* **333**, 209-213, (2011).

92. Lu, Z. & Stahl, S. S. Intramolecular Pd(II)-catalyzed aerobic oxidative amination of alkenes: synthesis of six-membered N-heterocycles. *Organic Letters* **14**, 1234-1237, (2012).

93. Pun, D., Diao, T. & Stahl, S. S. Aerobic dehydrogenation of cyclohexanone to phenol catalyzed by Pd(TFA)(2)/2-dimethylaminopyridine: evidence for the role of Pd nanoparticles. *Journal of the American Chemical Society* **135**, 8213-8221, (2013).

94. Gopidas, K. R., Whitesell, J. K. & Fox, M. A. Synthesis, characterization, and catalytic applications of a palladium-nanoparticle-cored dendrimer. *Nano Letters* **3**, 1757-1760, (2003).

95. Fang, T. *et al.* 3-Mercaptobutyric acid as an effective capping agent for highly luminescent CdTe quantum dots: new insight into the selection of mercapto acids. *Journal of Physical Chemistry C* **116**, 12346-12352, (2012).

96. Ruan, L. *et al.* Tailoring molecular specificity toward a crystal facet: a lesson from biorecognition toward Pt{111}. *Nano Letters* **13**, 840-846, (2013).

97. Hoeschele, J. D., Turner, J. E. & England, M. W. Inorganic concepts relevant to metal-binding, acticity , and toxicity in a biological system. *Science of the Total Environment* **109**, 477-492, (1991).

98. Liu, J., He, F., Durham, E., Zhao, D. & Roberts, C. B. Polysugar-stabilized Pd nanoparticles exhibiting high catalytic activities for hydrodechlorination of environmentally deleterious trichloroethylene. *Langmuir* **24**, 328-336, (2008).

99. Wang, Z., Zhang, Z. G. & Lu, X. Y. Effect of halide ligands on the reactivity of carbon-palladium bonds: Implications for designing catalytic reactions. *Organometallics* **19**, 775-780, (2000).

100. Zhang, Z. G., Lu, X. Y., Xu, Z. R., Zhang, Q. H. & Han, X. L. Role of halide ions in divalent palladium-mediated reactions: Competition between beta-heteroatom elimination and beta-hydride elimination of a carbon-palladium bond. *Organometallics* **20**, 3724-3728, (2001).

101. ten Brink, G. J., Arends, I. & Sheldon, R. A. Green, catalytic oxidation of alcohols in water. *Science* **287**, 1636-1639 (2000).

102. Steinhoff, B. A. & Stahl, S. S. Ligand-modulated palladium oxidation catalysis: Mechanistic insights into aerobic alcohol oxidation with the Pd(OAc)(2)/pyridine catalyst system. *Organic Letters* **4**, 4179-4181, (2002).

103. Sheldon, R. A., Arends, I., Ten Brink, G. J. & Dijksman, A. Green, catalytic oxidations of alcohols. *Accounts of Chemical Research* **35**, 774-781, (2002).